Geophysical Journal International

*Geophys. J. Int.* (2022) **231,** 1479–1501
Advance Access publication 2022 July 8
GJI Marine Geosciences and Applied Geophysics

https://doi.org/10.1093/gji/ggac261

# Effect of mesoscopic-flow loss on seismic reflections in media with penny-shaped inclusions

Enjiang Wang,[1,2] Lin Zhang,[3] José M. Carcione[3,4] and Jing Ba[3]

[1] *Key Lab of Submarine Geosciences and Prospecting Techniques, MOE, College of Marine Geosciences, Ocean University of China, Qingdao* 266100*, China*
[2] *Evaluation and Detection Technology Laboratory of Marine Mineral Resources, Qingdao National Laboratory for Marine Science and Technology, Qingdao* 266061*, China*
[3] *School of Earth Sciences and Engineering, Hohai University, Nanjing* 211100*, China. E-mail: jba@hhu.edu.cn*
[4] *National Institute of Oceanography and Applied Geophysics - OGS, Trieste, Italy*

Accepted 2022 July 6. Received 2022 May 30; in original form 2022 March 10

## SUMMARY

We obtain the amplitude and energy reflection coefficients of seismic waves in porous media with penny-shaped inclusions, based on the generalized Biot-Rayleigh model that takes into account the attenuation due to mesoscopic local fluid flow (LFF). We consider two cases, including a contact between two porous media having either different fluids (gas–water contact) or crack density and aspect ratio, as well as a water half-space overlying a porous medium, and study the frequency-dependent reflection-transmission (scattering) coefficients for open- and sealed-pore boundary conditions. Our examples show that the LFF mechanism mainly reduces the reflection coefficients (amplitude and energy) at the gas–water contact and at a water–porous medium interface for frequencies less than 10 kHz, due to the fact that the velocity in the lower medium decreases. For the latter case, if the fluid is gas, the LFF effect becomes only important at frequencies between 0.0001 and 10 Hz for the open-pore case. This is due to the fact that the acoustic impedance contrast between water and gas is high. At frequencies less than 0.0001 Hz, the interface is equivalent to a water–elastic medium one, and hence the results are the same as those of the sealed-pore case. Moreover, the crack density and aspect ratio affect the mesoscopic attenuation and relaxation frequency, and therefore the reflection coefficients.

**Key words:** Elasticity and anelasticity; Computational seismology; Seismic attenuation; Wave propagation.

## 1 INTRODUCTION

Wave propagation in porous media finds application in a variety of fields, such as seismology, hydrogeology and hydrocarbon exploration (Russell *et al.* 2011; Zong *et al.* 2012; Sharma 2013), to map the subsurface properties, such as porosity and saturation, which is essential for accurate reservoir characterization and fluid identification (Russell *et al.* 2011). Particularly, the presence of fluids induces attenuation and velocity dispersion by wave-induced fluid flow, which occurs when a wave creates pore pressure gradients. Based on the length scale of these gradients, the fluid flow can be classified as global (macro), squirt (micro) and mesoscopic (Pride *et al.* 2004; Carcione *et al.* 2010; Müller *et al.* 2010; Carcione & Gurevich 2011).

Global flow occurs when pressure gradients between peaks and troughs of the wave are induced, and attenuation is significant at frequencies above 100 kHz (Biot 1956, 1962). Biot's theory predicts a slow wave, which is diffusive at low frequencies and wavelike at high frequencies. The reflection problem was studied by Deresiewicz & Rice (1964), Dutta & Odé (1983), Gurevich *et al.* (2004), Liu *et al.* (2021) and Qi *et al.* (2021). A review of several expressions of the normal-incidence reflection coefficient was recently performed by Carcione *et al.* (2021), whereas the effect of the boundary conditions was analysed by Qi *et al.* (2021). These works yield a significant frequency dependence of the coefficients at high frequencies. The interface between a liquid and a liquid-saturated porous medium was considered in Santos *et al.* (1992), Denneman *et al.* (2002), Rubino *et al.* (2006), Bouzidi & Schmitt (2012) and Qi *et al.* (2021). In particular, when gas is present, the reflection coefficients depart from those of a single-phase medium, where the flow is not considered (Denneman *et al.* 2002).

On the other hand, squirt-flow loss occurs at the microscopic pore scale, due to the different compliances of cracks and stiff pores. It is significant at ultrasonic frequencies (Mavko & Nur 1975; Mavko & Jizba 1991; Dvorkin & Nur 1993; Chapman *et al.* 2002; Gurevich *et al.* 2010; Carcione & Gurevich 2011). In particular, Dvorkin & Nur (1993) proposed a dynamic poroelastic model that unified the Biot and squirt-flow loss mechanisms. Based on it, Cui & Wang (2003) considered an open-pore interface between a fluid and a fluid-saturated poroelastic solid, and studied the effect of squirt flow.

Mesoscopic-flow loss is due to heterogeneities on a scale much larger than the pore size but smaller than the wavelength (Pride *et al.* 2004; Carcione & Picotti 2006; Müller *et al.* 2010). It is widely accepted as the dominant mechanism for attenuation at seismic frequencies. The double-porosity theory is a simple and effective model to explain this phenomenon. Pride & Berryman (2003a, 2003b) presented a model, where the storage and fracture porosities coexist and a frequency-dependent compressibility law is introduced to describe the fluid transfer between these two pore spaces. The theory predicts realistic attenuation at the exploration-geophysics band. In addition, Ba *et al.* (2011) developed another double-porosity model based on the Biot theory of poroelasticity and the Rayleigh model of bubble oscillations. Scattering coefficients were studied by Dai & Kuang (2008) and Zhao *et al.* (2015). Sharma (2013) and Wang *et al.* (2020) investigated the effect of mesoscopic local fluid flow (LFF) on seismic reflections from the free surface of a double-porosity medium, and from an interface between two media, respectively. Basically, the LFF affects the energy partitions at the interface due to the mode transfer between the slow and fast waves, causing significant dispersion at low frequencies.

Cracks, which here refer to grain contacts or intragranular microfractures with an aspect ratio between $10^{-5}$ to $10^{-2}$, coexist with stiff pores in rocks. They play an important role in wave propagation, affecting not only the properties of the skeleton, but also the flow. Particularly, significant LFF occurs when the flow occurs between compliant cracks and relatively stiff pores, because of their dissimilar porosities, permeabilities, and compressibilities (Müller *et al.* 2010). This mechanism coexists with the Biot global flow. Tang (2011) and Tang *et al.* (2012) included the effects of cracks into the Biot model, and formulated a set of equations having as input parameters measurable properties such as the crack density and aspect ratio, which control the relaxation frequency and attenuation. The theory correctly predicts the velocity variation with gas saturation, but it is not compatible with Gassmann equation. Chapman *et al.* (2002) derived a Gassmann-consistent squirt flow model in which microstructure is assumed to consist of randomly oriented thin cracks and spherical pores. More models consider the anisotropy induced by the presence of cracks (Galvin & Gurevich 2009; Guo *et al.* 2018; Guo & Gurevich 2020). Based on the solution of the scattering problem for a single-crack and multiple-scattering theory, Galvin & Gurevich (2009) analysed the attenuation in a medium containing aligned sparsely distributed penny-shaped cracks. Fu *et al.* (2018) considered aligned silt cracks and presented an alternative solution of the scattering problem for a single crack and using the Waterman–Truell scattering approximation for a distribution of cracks. The estimated attenuation is proved similar to that of the penny-shaped case and the theory is consistent with the anisotropic Gassmann theory. Xu *et al.* (2021) considered fractures of different orientations embedded in layered rocks, and studied the frequency-dependent seismic properties, where the dual effects of the wave-induced fluid flow between the fractures and pores as well as between different layers are taken into account.

Zhang *et al.* (2019) represented the cracks as randomly oriented penny-shaped inclusions, and formulated a system of double-porosity equations in the framework of Hamilton's principle, generalizing Biot–Rayleigh model (Ba *et al.* 2011) from spherical inclusions to cylindrical cracks. The microvelocity field inside the cracks during the LFF process is considered. It is consistent with Gassmann equation and honours experimental data. Based on this approach, Kumari & Kumar (2020, 2021) studied the reflection of inhomogeneous waves at the free surface of a cracked medium, and analysed the contributions of reflected longitudinal waves to wave-induced LFF. To further understand the influence of LFF on wave propagation in cracked media, we consider two cases commonly encountered in exploration geophysics, namely, a contact between two cracked porous media and a fluid overlying a saturated medium. Unlike the work by Kumari & Kumar (2020), we represent the waves with Helmholtz potentials, which are determined from the uniform-porosity equations, so as to avoid restriction on the displacements. Based on the boundary conditions at the interfaces (either open or sealed), we derive the solutions of the scattering coefficients and energy ratios corresponding to the reflected and transmitted waves for an incident *P* wave.

## 2 GOVERNING DIFFERENTIAL EQUATIONS

As in Zhang *et al.* (2019), we consider randomly oriented cracks as penny-shaped inclusions embedded into a host medium, with two porosities and the same fluid, namely a local porosity $\phi_{10}$ of the host medium with a large volume fraction $f_1$, and a local porosity $\phi_{20}$ of the inclusions (cracks) with a smaller volume fraction $f_2 = 1 - f_1$ (see Fig. 1). The cracks have a radius $R_0$ and height $h$ and are much smaller than the wavelength, which corresponds to a mesoscopic-scale length. The boundary conditions between the inclusions and host medium are assumed open so that the mesoscopic-scale LFF takes place due to the contrasts in permeability and compressibility. The flow occurs mainly along the radial direction and is described by a generalization of Rayleigh's theory of liquid collapse of a spherical cavity to the penny-shaped case. The governing equations have as input parameters measurable properties such as the crack radius, density and aspect ratio, which highly affect the anelastic wave propagation.

The Lagrangian formulation proposed by Zhang *et al.* (2019) holds for non-uniform porosity because the relative fluid displacements are used as Lagrangian coordinates, and the total stress components and fluid pressure as generalized forces. With $\mathbf{u}$, $\mathbf{U}^{(1)}$ and $\mathbf{U}^{(2)}$ denoting the averaged displacement vectors of the matrix, fluid in host medium, and fluid in cracks, respectively, the relative fluid displacement vectors are

$$\mathbf{w}^{(m)} = \phi_m(\mathbf{U}^{(m)} - \mathbf{u}), \quad m = 1, 2 \tag{1}$$

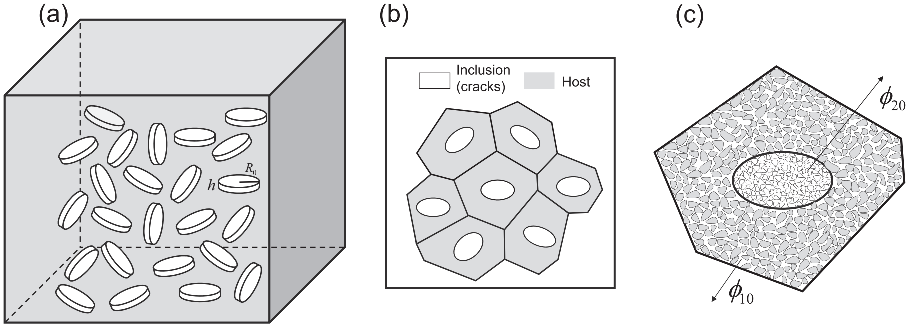

**Figure 1.** Schemes showing a cracked double-porosity medium. (a) Randomly oriented penny-shaped inclusions (cracks). (b) and (c) Penny-shaped cracks embedded into a host medium, with two porosities $\phi_{10}$ (host) and $\phi_{20}$ (cracks).

where $m = 1, 2$ represent the host medium and inclusions, and $\phi_m = f_m\phi_{m0}$ are the respective porosities. The strain–displacement relations are

$$\epsilon_{ij} = \frac{1}{2}(\partial_i u_j + \partial_j u_i), \quad \epsilon = \nabla \cdot \mathbf{u}, \quad \eta^{(m)} = \nabla \cdot \mathbf{U}^{(m)}, \quad m = 1, 2 \tag{2}$$

where $\epsilon_{ij}$ are the solid strain components, $\epsilon$ and $\eta^{(m)}$ are the averaged volumetric strains of the solid and the two variations of fluid content in the host ($m = 1$) and inclusions ($m = 2$). Using eq. (1), the two variations of fluid content relative to the solid are

$$\xi^{(m)} = -\nabla \cdot \mathbf{w}^{(m)} = -\phi_m(\eta^{(m)} - \epsilon), \quad m = 1, 2 \tag{3}$$

Let $\tau_{ij}$ be the total stress, $P_{\mathrm{f}m}$ the pore–fluid pressure in each phase and $\varsigma$ the fluid variation between the host medium and the penny-shaped inclusions. Then, the stress–strain relations are

$$\begin{aligned}
\tau_{ij} &= 2\mu_b\epsilon_{ij} + (\lambda_c\epsilon - \alpha_1 M_1(\xi^{(1)} - \phi_1\phi_2\varsigma) - \alpha_2 M_2(\xi^{(2)} + \phi_1\phi_2\varsigma))\delta_{ij},\\
P_{\mathrm{f}1} &= -\alpha_1 M_1\epsilon + M_1(\xi^{(1)} - \phi_1\phi_2\varsigma),\\
P_{\mathrm{f}2} &= -\alpha_2 M_2\epsilon + M_2(\xi^{(2)} + \phi_1\phi_2\varsigma),
\end{aligned} \tag{4}$$

where $\delta_{ij}$ is the Kronecker delta, with subscripts $i$ and $j$ being the Cartesian coordinates, $\mu_b$ is the dry-rock shear modulus and $\lambda_c$, $\alpha_1$, $\alpha_2$, $M_1$ and $M_2$ are stiffness coefficients, given in Appendix A.

The equations of motion are

$$\begin{aligned}
\tau_{ij,j} &= \rho\ddot{u}_i + \rho_{\mathrm{f}}\ddot{w}_i^{(1)} + \rho_{\mathrm{f}}\ddot{w}_i^{(2)},\\
-(P_{\mathrm{f}1})_{,i} &= \rho_{\mathrm{f}}\ddot{u}_i + m_1\ddot{w}_i^{(1)} + \frac{\eta\phi_{10}}{\kappa_1\phi_1}\dot{w}_i^{(1)},\\
-(P_{\mathrm{f}2})_{,i} &= \rho_{\mathrm{f}}\ddot{u}_i + m_2\ddot{w}_i^{(2)} + \frac{\eta\phi_{20}}{\kappa_2\phi_2}\dot{w}_i^{(2)},
\end{aligned} \tag{5}$$

where the comma preceding an index indicates spatial differentiation, the dot above a variable the time derivative, $\kappa_1$ and $\kappa_2$ are the permeabilities of the host medium and inclusions, respectively, $\eta$ is the fluid viscosity, $\rho_{\mathrm{f}}$ is the fluid density, $\rho = (1 - \phi)\rho_{\mathrm{s}} + \phi\rho_{\mathrm{f}}$ is the bulk density, with $\rho_{\mathrm{s}}$ being the grain density, $m_1 = \frac{\tau_1\rho_{\mathrm{f}}}{\phi_1}$, $m_2 = \frac{\tau_2\rho_{\mathrm{f}}}{\phi_2}$ are the Biot mass coefficients, where $\tau_m = \frac{1}{2}(1 + \frac{1}{\phi_{m0}})$ are the tortuosities (Berryman 1979).

The LFF governing equation for $\varsigma$ is obtained with a generalization of the Biot–Rayleigh theory (Ba *et al.* 2011) from spherical inclusions to cylindrical cracks. It is derived from the Lagrange equations based on the strain and kinetic energies and dissipation potential, where the microvelocity fields inside the inclusions are considered. The equation is

$$\begin{aligned}
&\left(\frac{3}{8} + \frac{\phi_{20}}{2\phi_{10}}\ln\frac{L + R_0}{R_0}\right)\phi_1^2\phi_2\rho_{\mathrm{f}}R_0^2\ddot{\varsigma} + \left(\frac{3\eta}{8\kappa_2} + \frac{\eta}{2\kappa_1}\ln\frac{L + R_0}{R_0}\right)\phi_{20}\phi_1^2\phi_2R_0^2\dot{\varsigma}\\
&\quad = \phi_1\phi_2(\alpha_1M_1 - \alpha_2M_2)\epsilon + \phi_1\phi_2(M_2\xi^{(2)} - M_1\xi^{(1)}) + \phi_1^2\phi_2^2(M_1 + M_2)\varsigma,
\end{aligned} \tag{6}$$

where $L = (R_0^2/12)^{1/2}$ is the characteristic fluid flow length.

Now, we recast the equations in the uniform-porosity formulation. Let $\sigma_{ij}$ and $\sigma_m$ be the solid stress components and fluid stresses in the two phases. Following Carcione (2014), they can be expressed as

$$\sigma_{ij} = \tau_{ij} - (\sigma_1 + \sigma_2)\delta_{ij}, \quad \sigma_m = -\phi_m P_{fm}, \quad m = 1, 2 \tag{7}$$

Using eqs (4) and (7), we have

$$\begin{aligned}\sigma_1 &= Q_1\epsilon + R_1(\eta^{(1)} + \phi_2\varsigma),\\ \sigma_2 &= Q_2\epsilon + R_2(\eta^{(2)} - \phi_1\varsigma),\\ \sigma_{ij} &= 2N\epsilon_{ij} + \left[A\epsilon + Q_1(\eta^{(1)} + \phi_2\varsigma) + Q_2(\eta^{(2)} - \phi_1\varsigma)\right]\delta_{ij},\end{aligned} \tag{8}$$

where $Q_m$ represent the coupling between the volume change of the solid and that of the fluid, $R_m$ are the pressures required on the fluid to inject a given volume of fluid into the aggregate whereas the total volume remains constant and $A$ and $N$ are the composite moduli equivalent to the Lamé constants in the theory of elasticity (Biot 1962). They can be expressed in terms of $\lambda_c$, $\alpha_m$ and $M_m$, as given in Appendix A.

From eqs (3) and (6), the corresponding LFF equation becomes

$$\begin{aligned}&\left(\frac{3}{8} + \frac{\phi_{20}}{2\phi_{10}}\ln\frac{L+R_0}{R_0}\right)\phi_1^2\phi_2\rho_{\mathrm{f}}R_0^2\ddot{\varsigma} + \left(\frac{3\eta}{8\kappa_2} + \frac{\eta}{2\kappa_1}\ln\frac{L+R_0}{R_0}\right)\phi_{20}\phi_1^2\phi_2R_0^2\dot{\varsigma}\\ &\quad = \left[\phi_2Q_1 - \phi_1Q_2\right]\epsilon + \phi_2R_1\eta^{(1)} - \phi_1R_2\eta^{(2)} + (\phi_2^2R_1 + \phi_1^2R_2)\varsigma.\end{aligned} \tag{9}$$

Similarly, the equations of momentum conservation corresponding to (5) are

$$\begin{aligned}\sigma_{ij,j} &= \rho_{00}\ddot{u}_i + \rho_{01}\ddot{U}_i^{(1)} + \rho_{02}\ddot{U}_i^{(2)} + b_1(\dot{u}_i - \dot{U}_i^{(1)}) + b_2(\dot{u}_i - \dot{U}_i^{(2)}),\\ (\sigma_1)_{,i} &= \rho_{01}\ddot{u}_i + \rho_{11}\ddot{U}_i^{(1)} - b_1(\dot{u}_i - \dot{U}_i^{(1)}),\\ (\sigma_2)_{,i} &= \rho_{02}\ddot{u}_i + \rho_{22}\ddot{U}_i^{(2)} - b_2(\dot{u}_i - \dot{U}_i^{(2)}),\end{aligned} \tag{10}$$

where $b_1 = \phi_1\phi_{10}\eta/\kappa_1$ and $b_2 = \phi_2\phi_{20}\eta/\kappa_2$ are the viscous couplings between the pore fluid and skeleton, and $\rho_{ij}$ are five density parameters, given in Appendix A.

## 3 PLANE-WAVE SOLUTION

By substituting eqs (7) and (8) into (10), we obtain

$$\begin{aligned}&N\nabla^2\mathbf{u} + (A+N)\nabla\epsilon + Q_1\nabla(\eta^{(1)} + \phi_2\varsigma) + Q_2\nabla(\eta^{(2)} - \phi_1\varsigma) = \rho_{00}\ddot{\mathbf{u}} + \rho_{01}\ddot{\mathbf{U}}^{(1)} + \rho_{02}\ddot{\mathbf{U}}^{(2)} + b_1(\dot{\mathbf{u}} - \dot{\mathbf{U}}^{(1)}) + b_2(\dot{\mathbf{u}} - \dot{\mathbf{U}}^{(2)}),\\ &Q_1\nabla\epsilon + R_1\nabla(\eta^{(1)} + \phi_2\varsigma) = \rho_{01}\ddot{\mathbf{u}} + \rho_{11}\ddot{\mathbf{U}}^{(1)} - b_1(\dot{\mathbf{u}} - \dot{\mathbf{U}}^{(1)}),\\ &Q_2\nabla\epsilon + R_2\nabla(\eta^{(2)} - \phi_1\varsigma) = \rho_{02}\ddot{\mathbf{u}} + \rho_{22}\ddot{\mathbf{U}}^{(2)} - b_2(\dot{\mathbf{u}} - \dot{\mathbf{U}}^{(2)}).\end{aligned} \tag{11}$$

Eqs (9) and (11) are the governing equations for wave propagation in terms of the displacements $\mathbf{u}$, $\mathbf{U^{(1)}}$ and $\mathbf{U^{(2)}}$. Considering time harmonic oscillations (the Fourier convention is $\exp[-\mathrm{i}\omega t]$), based on eq. (9), we have

$$\varsigma = d_1\epsilon + d_2\eta^{(1)} + d_3\eta^{(2)}, (d_1, d_2, d_3) = (\phi_1Q_2 - \phi_2Q_1, -\phi_2R_1, \phi_1R_2)/(L_1\omega^2 + L_2\mathrm{i}\omega + \phi_2^2R_1 + \phi_1^2R_2), \tag{12}$$

where $L_1 = \left(\frac{3}{8} + \frac{\phi_{20}}{2\phi_{10}}\ln\frac{L+R_0}{R_0}\right)\phi_1^2\phi_2\rho_{\mathrm{f}}R_0^2$ and $L_2 = \left(\frac{3\eta}{8\kappa_2} + \frac{\eta}{2\kappa_1}\ln\frac{L+R_0}{R_0}\right)\phi_{20}\phi_1^2\phi_2R_0^2$.

Substituting eq. (12) into (11), and after a simplification, we have

$$\begin{aligned}&N\nabla^2\mathbf{u} + (A + N + Zd_1)\nabla\epsilon + (Q_1 + Zd_2)\nabla\eta^{(1)} + (Q_2 + Zd_3)\nabla\eta^{(2)} = \rho_{00}\ddot{\mathbf{u}} + \rho_{01}\ddot{\mathbf{U}}^{(1)} + \rho_{02}\ddot{\mathbf{U}}^{(2)} + b_1(\dot{\mathbf{u}} - \dot{\mathbf{U}}^{(1)}) + b_2(\dot{\mathbf{u}} - \dot{\mathbf{U}}^{(2)}),\\ &(Q_1 + R_1\phi_2d_1)\nabla\epsilon + (R_1 + R_1\phi_2d_2)\nabla\eta^{(1)} + R_1\phi_2d_3\nabla\eta^{(2)} = \rho_{01}\ddot{\mathbf{u}} + \rho_{11}\ddot{\mathbf{U}}^{(1)} - b_1(\dot{\mathbf{u}} - \dot{\mathbf{U}}^{(1)}),\\ &(Q_2 - R_2\phi_1d_1)\nabla\epsilon - R_2\phi_1d_2\nabla\eta^{(1)} + (R_2 - R_2\phi_1d_3)\nabla\eta^{(2)} = \rho_{02}\ddot{\mathbf{u}} + \rho_{22}\ddot{\mathbf{U}}^{(2)} - b_2(\dot{\mathbf{u}} - \dot{\mathbf{U}}^{(2)}),\end{aligned} \tag{13}$$

where $Z = Q_1\phi_2 - Q_2\phi_1$.

Using the Helmholtz decomposition, the displacement vectors $\mathbf{u}$, $\mathbf{U^{(1)}}$ and $\mathbf{U^{(2)}}$ can be expressed in terms of potential functions $\varphi_i$ and $\Psi_{\mathbf{i}}$ ($i = 0, 1, 2$), as follows:

$$\mathbf{u} = \nabla\varphi_0 + \nabla\times\Psi_{\mathbf{0}}, \quad \mathbf{U}^{(1)} = \nabla\varphi_1 + \nabla\times\Psi_{\mathbf{1}}, \quad \mathbf{U}^{(2)} = \nabla\varphi_2 + \nabla\times\Psi_{\mathbf{2}}, \tag{14}$$

where here the subscripts $i = 0, 1, 2$ correspond to the solid, fluid phase in the host medium and fluid phase in the inclusions (cracks), respectively.

Applying the divergence operator to eq. (13), we have

$$\begin{pmatrix}\rho_{00} & \rho_{01} & \rho_{02}\\ \rho_{01} & \rho_{11} & 0\\ \rho_{02} & 0 & \rho_{22}\end{pmatrix}\begin{pmatrix}\ddot{\varphi}_0\\ \ddot{\varphi}_1\\ \ddot{\varphi}_2\end{pmatrix} + \begin{pmatrix}b_1 + b_2 & -b_1 & -b_2\\ -b_1 & b_1 & 0\\ -b_2 & 0 & b_2\end{pmatrix}\begin{pmatrix}\dot{\varphi}_0\\ \dot{\varphi}_1\\ \dot{\varphi}_2\end{pmatrix} = \begin{pmatrix}A + 2N + Zd_1 & Q_1 + Zd_2 & Q_2 + Zd_3\\ Q_1 + R_1\phi_2d_1 & R_1 + R_1\phi_2d_2 & R_1\phi_2d_3\\ Q_2 - R_2\phi_1d_1 & -R_2\phi_1d_2 & R_2 - R_2\phi_1d_3\end{pmatrix}\begin{pmatrix}\nabla^2\varphi_0\\ \nabla^2\varphi_1\\ \nabla^2\varphi_2\end{pmatrix}, \tag{15}$$

corresponding to the $P$-wave potentials. Invoking the expressions of $Z$ and $d_i$, the matrix on the right-hand side of eq. (15) can be shown to be symmetric.

Similarly, after applying the curl operator, we obtain equations for the $S$-wave potentials as

$$\begin{pmatrix} \rho_{00} & \rho_{01} & \rho_{02} \\ \rho_{01} & \rho_{11} & 0 \\ \rho_{02} & 0 & \rho_{22} \end{pmatrix} \begin{pmatrix} \ddot{\Psi}_0 \\ \ddot{\Psi}_1 \\ \ddot{\Psi}_2 \end{pmatrix} + \begin{pmatrix} b_1+b_2 & -b_1 & -b_2 \\ -b_1 & b_1 & 0 \\ -b_2 & 0 & b_2 \end{pmatrix} \begin{pmatrix} \dot{\Psi}_0 \\ \dot{\Psi}_1 \\ \dot{\Psi}_2 \end{pmatrix} = \begin{pmatrix} N & 0 & 0 \\ 0 & 0 & 0 \\ 0 & 0 & 0 \end{pmatrix} \begin{pmatrix} \nabla^2\Psi_0 \\ \nabla^2\Psi_1 \\ \nabla^2\Psi_2 \end{pmatrix}. \tag{16}$$

The analytical plane-wave kernels for the potentials are

$$\begin{cases} \varphi_0 = A_0 \exp\left[\mathrm{i}(\mathbf{k_p}\cdot\mathbf{r} - \omega t)\right], \\ \varphi_1 = A_1 \exp\left[\mathrm{i}(\mathbf{k_p}\cdot\mathbf{r} - \omega t)\right], \\ \varphi_2 = A_2 \exp\left[\mathrm{i}(\mathbf{k_p}\cdot\mathbf{r} - \omega t)\right], \end{cases} \qquad \begin{cases} \Psi_0 = B_0 \exp\left[\mathrm{i}(\mathbf{k}_\mathrm{s}\cdot\mathbf{r} - \omega t)\right], \\ \Psi_1 = B_1 \exp\left[\mathrm{i}(\mathbf{k}_\mathrm{s}\cdot\mathbf{r} - \omega t)\right], \\ \Psi_2 = B_2 \exp\left[\mathrm{i}(\mathbf{k}_\mathrm{s}\cdot\mathbf{r} - \omega t)\right], \end{cases} \tag{17}$$

where $A_i$ and $B_i$ ($i = 0, 1, 2$) are amplitudes, $\omega$ is the angular frequency, $\mathbf{k_p}$ and $\mathbf{k}_\mathrm{s}$ are the wavenumbers of the compressional and shear waves, respectively, and $\mathbf{r}$ is the space vector.

Substituting eqs (17) into (15), we obtain

$$\mathbf{H}\cdot\mathbf{A} = \mathbf{0}, \tag{18}$$

where $\mathbf{A} = [A_0, A_1, A_2]^\mathrm{T}$, and the components of $\mathbf{H}$ are

$$\begin{cases} H_{11} = (A + 2N + Zd_1)k_p^2 - \rho_{00}\omega^2 - \mathrm{i}\omega(b_1 + b_2), \\ H_{12} = H_{21} = (Q_1 + Zd_2)k_p^2 - \rho_{01}\omega^2 + \mathrm{i}\omega b_1, \\ H_{13} = H_{31} = (Q_2 + Zd_3)k_p^2 - \rho_{02}\omega^2 + \mathrm{i}\omega b_2, \\ H_{22} = (R_1 + R_1\phi_2 d_2)k_p^2 - \rho_{11}\omega^2 - \mathrm{i}\omega b_1, \\ H_{23} = H_{32} = R_1\phi_2 d_3 k_p^2, \\ H_{33} = (R_2 - R_2\phi_1 d_3)k_p^2 - \rho_{22}\omega^2 - \mathrm{i}\omega b_2. \end{cases} \tag{19}$$

The condition $\det(\mathbf{H}) = 0$ gives three complex roots of the unknown wavenumbers $k_1$, $k_2$ and $k_3$, corresponding to the fast $P$ wave ($P1$) and two slow $P$ waves ($P2$ and $P3$). The related velocities, being complex, describe the attenuation characteristics. By solving eq. (18), the relative relations between the amplitudes of two fluid-phase potentials and that of the solid phase are

$$\begin{pmatrix} A_1/A_0 \\ A_2/A_0 \end{pmatrix} = \begin{pmatrix} (H_{13}H_{21} - H_{11}H_{23})/(H_{12}H_{23} - H_{13}H_{22}) \\ (H_{11}H_{22} - H_{21}H_{12})/(H_{12}H_{23} - H_{13}H_{22}) \end{pmatrix} = \begin{pmatrix} \nu \\ \delta \end{pmatrix}. \tag{20}$$

Because there are three compressional waves, the potentials are coupled as

$$\begin{cases} \varphi_\mathrm{s} = \varphi_\mathrm{I} + \varphi_\mathrm{II} + \varphi_\mathrm{III}, \\ \varphi_\mathrm{f1} = \nu_1\varphi_\mathrm{I} + \nu_2\varphi_\mathrm{II} + \nu_3\varphi_\mathrm{III}, \\ \varphi_\mathrm{f2} = \delta_1\varphi_\mathrm{I} + \delta_2\varphi_\mathrm{II} + \delta_3\varphi_\mathrm{III}, \end{cases} \tag{21}$$

where $\varphi_\mathrm{I}$, $\varphi_\mathrm{II}$ and $\varphi_\mathrm{III}$ are the solid-phase potentials of the $P1$, $P2$ and $P3$ waves specified with wavenumbers $k_1$, $k_2$ and $k_3$, respectively; $\nu_i$ and $\delta_i$ are amplitude ratios defined in eq. (20) using the wavenumber $k_i$, with '$s$', '$f1$' and '$f2$' denoting the solid and two fluid phases, respectively.

Similarly, substituting eq. (17) into (16) yields

$$\mathbf{Q}\cdot\mathbf{B} = \mathbf{0}, \tag{22}$$

where, $\mathbf{B} = [B_0, B_1, B_2]^\mathrm{T}$, and the components of $\mathbf{Q}$ are

$$\begin{cases} Q_{11} = Nk_\mathrm{s}^2 - \rho_{00}\omega^2 - \mathrm{i}\omega(b_1 + b_2), \\ Q_{12} = Q_{21} = -\rho_{01}\omega^2 + \mathrm{i}\omega b_1, \\ Q_{13} = Q_{31} = -\rho_{02}\omega^2 + \mathrm{i}\omega b_2, \\ Q_{22} = -\rho_{11}\omega^2 - \mathrm{i}\omega b_1, \\ Q_{23} = Q_{32} = 0, \\ Q_{33} = -\rho_{22}\omega^2 - \mathrm{i}\omega b_2. \end{cases} \tag{23}$$

The condition $\det(\mathbf{Q}) = 0$ gives one complex wavenumber (denoted as $k_4$), corresponding to the shear wave (SV), and the relative-amplitude ratio is

$$\begin{pmatrix} B_1/B_0 \\ B_2/B_0 \end{pmatrix} = \begin{pmatrix} -Q_{21}/Q_{22} \\ (Q_{21}Q_{12} - Q_{11}Q_{22})/(Q_{13}Q_{22}) \end{pmatrix} = \begin{pmatrix} \nu_4 \\ \delta_4 \end{pmatrix}. \tag{24}$$

Following Carcione (2014), the corresponding phase velocities and attenuation factors are given in terms of the complex wavenumber as,

$$V_i = \left[\mathrm{Re}\left(\frac{k_i}{\omega}\right)\right]^{-1}, \quad Q_i^{-1} = 2\frac{\mathrm{Im}(k_i)}{\mathrm{Re}(k_i)}, \quad i = 1, 2, 3, 4, \tag{25}$$

where 'Re' and 'Im' denote real and imaginary parts and indexes 1–4 indicate the wave modes $P1$, $P2$, $P3$ and SV, respectively.

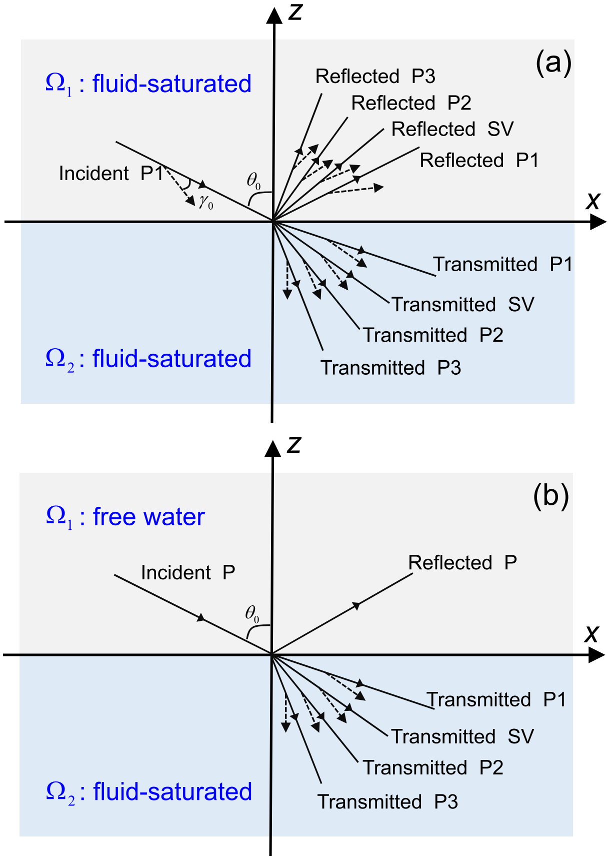

**Figure 2.** Reflection and transmission problem at a plane interface between (a) two fluid-saturated cracked media and (b) water half-space overlying a fluid-saturated cracked medium. The solid and dashed arrows represent the propagation and attenuation directions, respectively. *P*1, *P*2 and *P*3 represent the fast and two slow compressional wave modes in the porous medium, whereas SV indicates the shear wave mode.

## 4 SCATTERING (REFLECTION–TRANSMISSION) COEFFICIENTS

We consider two cases (see Fig. 2), namely, an interface separating two porous media, and an interface separating a fluid and a porous medium. The latter case can be used to estimate seafloor properties from reflected data (Qi *et al.* 2021). In the first case, we consider a gas–water contact (Dutta & Odé 1983), as well as a contact between two media having the same fluid but different rock frames.

### 4.1 Interface between two porous media

As shown in Fig. 2(a), we consider an interface defined by $z = 0$, separating two media $\Omega_1(z > 0)$ and $\Omega_2(z < 0)$, and a $P1$ wave (denoted with index 0) in $\Omega_1$ incident at the interface with an oblique angle. This wave generates four reflected waves ($P1$, $P2$, $P3$, SV, denoted with the indexes 1, 2, 3 and 4) in $\Omega_1$ and four transmitted waves ($P1$, $P2$, $P3$, SV, denoted with the indexes 5, 6, 7 and 8) in $\Omega_2$.

Due to the presence of wave-induced fluid flow, the media behave anelastic to wave propagation, implying that all the incident, reflected and transmitted waves are inhomogeneous, in the sense that the propagation and attenuation directions do not coincide. Following Carcione (2014), a general representation of an inhomogeneous wave can be specified by its direction of propagation as well as direction of maximum attenuation. For the incident $P1$ wave, we have

$$\begin{cases} \varphi_{\mathrm{s}}^{(0)} = A_{\mathrm{s}}^{(0)} \exp\left[\mathrm{i}\omega(p_0 x - q_0 z) - \mathrm{i}\omega t\right], \\ \varphi_{\mathrm{f1}}^{(0)} = \nu_1^{(\Omega_1)} A_{\mathrm{s}}^{(0)} \exp\left[\mathrm{i}\omega(p_0 x - q_0 z) - \mathrm{i}\omega t\right], \\ \varphi_{\mathrm{f2}}^{(0)} = \delta_1^{(\Omega_1)} A_{\mathrm{s}}^{(0)} \exp\left[\mathrm{i}\omega(p_0 x - q_0 z) - \mathrm{i}\omega t\right], \end{cases} \tag{26}$$

where $A_{\mathrm{s}}^{(0)}$ is the amplitude, $\nu_i^{(\Omega_1)}$ and $\delta_i^{(\Omega_1)}$ are the amplitude ratios in medium $\Omega_1$, determined in eq. (20) using wavenumber $k_i$ (here $i = 1$), and

$$p_0 = \frac{|\mathbf{P_0}|}{\omega}\sin\theta_0 + \mathrm{i}\frac{|\mathbf{A_0}|}{\omega}\sin(\theta_0 - \gamma_0), \tag{27}$$

is the horizontal complex slowness, where $\theta_0$ is the propagation direction, $\gamma_0$ is the inhomogeneity angle (Sharma 2013; Carcione 2014). The propagation vector $\mathbf{P_0}$ and attenuation vector $\mathbf{A_0}$ are obtained from

$$\begin{cases} 2|\mathbf{P_0}|^2 = \omega^2\left[\mathrm{Re}(v_0^{-2}) + \sqrt{\left(\mathrm{Re}(v_0^{-2})\right)^2 + \left(\mathrm{Im}(v_0^{-2})/\cos\gamma_0\right)^2}\right], \\ 2|\mathbf{A_0}|^2 = \omega^2\left[-\mathrm{Re}(v_0^{-2}) + \sqrt{\left(\mathrm{Re}(v_0^{-2})\right)^2 + \left(\mathrm{Im}(v_0^{-2})/\cos\gamma_0\right)^2}\right], \end{cases} \tag{28}$$

where $v_0 = \omega/k_1$ is the complex velocity of the incident $P1$ wave.

The vertical slowness is

$$q_0 = G_{\mathrm{R}} + \mathrm{i}G_{\mathrm{I}}, \quad G = \pm\mathrm{pv}\sqrt{v_0^{-2} - p_0^2}, \tag{29}$$

where 'pv' denotes the principal value and $G_{\mathrm{R}}$ and $G_{\mathrm{I}}$ are the real and imaginary parts of $G$, respectively. In this way, the sign for $q_0$ in eq. (26) is negative, which ensures the propagation and energy decay of the wave along the negative $z$-direction.

The potentials for the reflected waves are similarly written as

$$\begin{cases} \varphi_{\mathrm{s}}^{(i)} = A_{\mathrm{s}}^{(i)}\exp\left[\mathrm{i}\omega(p_i x + q_i z) - \mathrm{i}\omega t\right], \\ \varphi_{\mathrm{f1}}^{(i)} = \nu_i^{(\Omega_1)} A_{\mathrm{s}}^{(i)}\exp\left[\mathrm{i}\omega(p_i x + q_i z) - \mathrm{i}\omega t\right], \quad i = 1, 2, 3 \\ \varphi_{\mathrm{f2}}^{(i)} = \delta_i^{(\Omega_1)} A_{\mathrm{s}}^{(i)}\exp\left[\mathrm{i}\omega(p_i x + q_i z) - \mathrm{i}\omega t\right], \end{cases} \tag{30}$$

for the compressional $P1$, $P2$ and $P3$ waves with $i = 1, 2, 3$, respectively. For the reflected SV wave,

$$\begin{cases} \Psi_{\mathrm{s}}^{(4)} = A_{\mathrm{s}}^{(4)}\exp\left[\mathrm{i}\omega(p_4 x + q_4 z) - \mathrm{i}\omega t\right], \\ \Psi_{\mathrm{f1}}^{(4)} = \nu_4^{(\Omega_1)} A_{\mathrm{s}}^{(4)}\exp\left[\mathrm{i}\omega(p_4 x + q_4 z) - \mathrm{i}\omega t\right], \\ \Psi_{\mathrm{f2}}^{(4)} = \delta_4^{(\Omega_1)} A_{\mathrm{s}}^{(4)}\exp\left[\mathrm{i}\omega(p_4 x + q_4 z) - \mathrm{i}\omega t\right], \end{cases} \tag{31}$$

where, $\nu_4^{(\Omega_1)}$ and $\delta_4^{(\Omega_1)}$ are the amplitude ratios in medium $\Omega_1$, determined in eq. (24) using wavenumber $k_4$.

Similarly, the potentials for the transmitted waves are

$$\begin{cases} \varphi_{\mathrm{s}}^{(i)} = A_{\mathrm{s}}^{(i)}\exp\left[\mathrm{i}\omega(p_i x - q_i z) - \mathrm{i}\omega t\right], \\ \varphi_{\mathrm{f1}}^{(i)} = \nu_{i-4}^{(\Omega_2)} A_{\mathrm{s}}^{(i)}\exp\left[\mathrm{i}\omega(p_i x - q_i z) - \mathrm{i}\omega t\right], \quad i = 5, 6, 7 \\ \varphi_{\mathrm{f2}}^{(i)} = \delta_{i-4}^{(\Omega_2)} A_{\mathrm{s}}^{(i)}\exp\left[\mathrm{i}\omega(p_i x - q_i z) - \mathrm{i}\omega t\right], \end{cases} \tag{32}$$

for the transmitted $P1$, $P2$ and $P3$ waves with $i = 5, 6, 7$, respectively, and

$$\begin{cases} \Psi_{\mathrm{s}}^{(8)} = A_{\mathrm{s}}^{(8)}\exp\left[\mathrm{i}\omega(p_8 x - q_8 z) - \mathrm{i}\omega t\right], \\ \Psi_{\mathrm{f1}}^{(8)} = \nu_4^{(\Omega_2)} A_{\mathrm{s}}^{(8)}\exp\left[\mathrm{i}\omega(p_8 x - q_8 z) - \mathrm{i}\omega t\right], \\ \Psi_{\mathrm{f2}}^{(8)} = \delta_4^{(\Omega_2)} A_{\mathrm{s}}^{(8)}\exp\left[\mathrm{i}\omega(p_8 x - q_8 z) - \mathrm{i}\omega t\right], \end{cases} \tag{33}$$

for the transmitted SV wave, where $\nu_i^{(\Omega_2)}$ and $\delta_i^{(\Omega_2)}$, $i = 1, \ldots, 4$ are the amplitude ratios in medium $\Omega_2$.

Invoking the Snell law, the horizontal slowness satisfy

$$p_1 = p_2 = p_3 = p_4 = p_5 = p_6 = p_7 = p_8 = p_0. \tag{34}$$

Then, the vertical slowness can be obtained from the complex velocity $v_i = \omega/k_i$ as

$$q_i = G_{\mathrm{R}} + \mathrm{i}G_{\mathrm{I}}, G = \pm\mathrm{pv}\sqrt{v_i^{-2} - p_i^2}, \quad i = 1, 2, \ldots, 7, 8 \tag{35}$$

In medium $\Omega_1$, the positive signs for $q_i$ of the reflected waves in eqs (30) and (31) are chosen such that the propagation is along the positive $z$-direction and the energy decays away from the interface (Borcherdt 1982). In medium $\Omega_2$, the signs for $q_i$ of the transmitted waves in eqs (32) and (33) are negative to ensure that the propagation is along the negative $z$-direction and the energy decays away from the interface.

Substituting the potential functions into the Helmholtz equation, we obtain

$$\begin{cases} \mathbf{u}^{\Omega_1} = \nabla(\varphi_{\mathrm{s}}^{(0)} + \varphi_{\mathrm{s}}^{(1)} + \varphi_{\mathrm{s}}^{(2)} + \varphi_{\mathrm{s}}^{(3)}) + \left[-\dfrac{\partial\Psi_{\mathrm{s}}^{(4)}}{\partial z}, \dfrac{\partial\Psi_{\mathrm{s}}^{(4)}}{\partial x}\right]^{\mathrm{T}}, \\ \mathbf{U}^{\Omega_1,(1)} = \nabla(\varphi_{\mathrm{f1}}^{(0)} + \varphi_{\mathrm{f1}}^{(1)} + \varphi_{\mathrm{f1}}^{(2)} + \varphi_{\mathrm{f1}}^{(3)}) + \left[-\dfrac{\partial\Psi_{\mathrm{f1}}^{(4)}}{\partial z}, \dfrac{\partial\Psi_{\mathrm{f1}}^{(4)}}{\partial x}\right]^{\mathrm{T}}, \\ \mathbf{U}^{\Omega_1,(2)} = \nabla(\varphi_{\mathrm{f2}}^{(0)} + \varphi_{\mathrm{f2}}^{(1)} + \varphi_{\mathrm{f2}}^{(2)} + \varphi_{\mathrm{f2}}^{(3)}) + \left[-\dfrac{\partial\Psi_{\mathrm{f2}}^{(4)}}{\partial z}, \dfrac{\partial\Psi_{\mathrm{f2}}^{(4)}}{\partial x}\right]^{\mathrm{T}}, \end{cases} \tag{36}$$

for medium $\Omega_1$, and

$$\begin{cases} \mathbf{u}^{\Omega_2} = \nabla(\varphi_{\rm s}^{(5)} + \varphi_{\rm s}^{(6)} + \varphi_{\rm s}^{(7)}) + \left[-\dfrac{\partial \Psi_{\rm s}^{(8)}}{\partial z}, \dfrac{\partial \Psi_{\rm s}^{(8)}}{\partial x}\right]^{\rm T}, \\ \mathbf{U}^{\Omega_2,(1)} = \nabla(\varphi_{\rm f1}^{(5)} + \varphi_{\rm f1}^{(6)} + \varphi_{\rm f1}^{(7)}) + \left[-\dfrac{\partial \Psi_{\rm f1}^{(8)}}{\partial z}, \dfrac{\partial \Psi_{\rm f1}^{(8)}}{\partial x}\right]^{\rm T}, \\ \mathbf{U}^{\Omega_2,(2)} = \nabla(\varphi_{\rm f2}^{(5)} + \varphi_{\rm f2}^{(6)} + \varphi_{\rm f2}^{(7)}) + \left[-\dfrac{\partial \Psi_{\rm f2}^{(8)}}{\partial z}, \dfrac{\partial \Psi_{\rm f2}^{(8)}}{\partial x}\right]^{\rm T}, \end{cases} \tag{37}$$

for medium $\Omega_2$. By substituting eqs (36) and (37) into (4), the expressions for the stresses $\tau_{ij}$ and fluid pressures $P_{\rm f1}$ and $P_{\rm f2}$ in media $\Omega_1$ and $\Omega_2$ can be obtained.

There are eight unknown amplitudes of the potentials $A_{\rm s}^{(i)}$, $i = 1, 2, \ldots, 8$, which can be determined via eight boundary conditions (BCs) at $z = 0$. Following Deresiewicz & Skalak (1963), these conditions are

$$\begin{cases} \tau_{xz}^{\Omega_1} = \tau_{xz}^{\Omega_2}, \\ \tau_{zz}^{\Omega_1} = \tau_{zz}^{\Omega_2}, \\ u_x^{\Omega_1} = u_x^{\Omega_2}, \\ u_z^{\Omega_1} = u_z^{\Omega_2}, \\ w_z^{\Omega_1,(1)} = w_z^{\Omega_2,(1)}, \\ w_z^{\Omega_1,(2)} = w_z^{\Omega_2,(2)}, \\ P_{\rm f1}^{\Omega_1} - P_{\rm f1}^{\Omega_2} = Z_I \dot{w}_z^{\Omega_2,(1)}, \\ P_{\rm f2}^{\Omega_1} - P_{\rm f2}^{\Omega_2} = Z_I \dot{w}_z^{\Omega_2,(2)}, \end{cases} \tag{38}$$

where $Z_{\rm I}$ is the so-called interface impedance. If $Z_{\rm I} = 0$, the boundary becomes fully open, that is perfect hydraulic contact. If $Z_{\rm I} = \infty$, eq. (38) becomes the sealed-pore boundary condition, where no relative fluid flow takes place across the interface.

The eight boundary conditions result in a system of linear equations, which has the matrix form

$$\sum_{j=1}^{8} G_{ij} y_j = e_i, \quad i = 1, 2, \ldots, 7, 8, \tag{39}$$

where $\mathbf{y}$ consists of the eight unknown amplitudes of the displacement potentials, that is $y_j = A_{\rm s}^{(j)}$. The explicit expressions for the elements of $\mathbf{G}$ and vector $\mathbf{e}$ are given in Appendix B. Once $\mathbf{y}$ is solved, the $R/T$ coefficients can be obtained as

$$\begin{aligned} R_j &= \frac{A_{\rm s}^{(j)} k_j}{A_{\rm s}^{(0)} k_1} = |R_j| e^{{\rm i}\theta_j}, \; j = 1, 2, 3, 4, \\ T_j &= \frac{A_{\rm s}^{(j)} k_j}{A_{\rm s}^{(0)} k_1} = |T_j| e^{{\rm i}\theta_j}, \; j = 5, 6, 7, 8, \end{aligned} \tag{40}$$

which are defined as the ratio of the solid displacement amplitude of a reflected or transmitted wave to that of the incident wave. The $|R_j|$ and $|T_j|$ represent the magnitudes, whereas $\theta_j$ defines the phase angle.

### 4.2 Interface between a fluid and a porous medium

Fig. 2(b) illustrates the problem. The incident wave (denoted with index 0) is homogeneous and hits the interface at the angle $\theta_0$, generating a reflected homogeneous wave (denoted with index 1) in medium $\Omega_1$ and four transmitted inhomogeneous waves (denoted with indexes 5, 6, 7 and 8 for $P1$, $P2$, $P3$ and SV waves, respectively) in medium $\Omega_2$. The displacement potential of the incident wave is

$$\varphi_{\rm s}^{(0)} = A_{\rm s}^{(0)} \exp\left[{\rm i}\omega(p_0 x - q_0 z) - {\rm i}\omega t\right], \tag{41}$$

where

$$p_0 = \frac{\sin\theta_0}{v_0}, \quad q_0 = \frac{\cos\theta_0}{v_0}, \tag{42}$$

$v_0 = \sqrt{\dfrac{K_{\rm f}}{\rho_{\rm f}}}$ is the fluid velocity and $\theta_0$ is the incidence angle.

The potential of the reflected wave is

$$\varphi_{\rm s}^{(1)} = A_{\rm s}^{(1)} \exp\left[{\rm i}\omega(p_0 x + q_0 z) - {\rm i}\omega t\right], \tag{43}$$

where the positive sign for $q_0$ indicates that the wave propagates along the positive $z$-direction. The four transmitted waves are inhomogeneous and have the same form of eqs (32) and (33) and eqs (34) and (35) hold.

From eqs (41) and (43), the $P$-wave displacement in the fluid is

$$\mathbf{U}^{\Omega_1} = \nabla(\varphi_{\rm s}^{(0)} + \varphi_{\rm s}^{(1)}). \tag{44}$$

Then, the fluid pressure is

$$p_{\mathrm{f}} = -K_{\mathrm{f}} \nabla \cdot \mathbf{U}^{\Omega_1}. \tag{45}$$

The corresponding boundary conditions become

$$\begin{cases} \tau_{xz}^{\Omega_2} = 0, \\ -p_{\mathrm{f}}^{\Omega_1} = \tau_{zz}^{\Omega_2}, \\ U_z^{\Omega_1} = u_z^{\Omega_2} + w_z^{\Omega_2,(1)} + w_z^{\Omega_2,(2)}, \\ p_f^{\Omega_1} - P_{\mathrm{f1}}^{\Omega_2} = Z_I \dot{w}_z^{\Omega_2,(1)}, \\ p_f^{\Omega_1} - P_{\mathrm{f2}}^{\Omega_2} = Z_I \dot{w}_z^{\Omega_2,(2)}. \end{cases} \tag{46}$$

The first three equations represent the continuity of the normal and shear stresses and the conservation of mass. The last two describe the natural BCs for the fluid pressure, where, $Z_{\mathrm{I}} = 0$ and $Z_{\mathrm{I}} = \infty$ correspond to open and sealed boundary conditions, respectively (Qi *et al.* 2021). These five BCs form a system of linear equations, from which the *R*/*T* coefficients can be determined. The matrix form is

$$\sum_{j=1}^{5} M_{ij} x_j = c_i, \quad i = 1, 2, \ldots, 5, \tag{47}$$

where $\mathbf{x} = [A_{\mathrm{s}}^{(1)}, A_{\mathrm{s}}^{(5)}, A_{\mathrm{s}}^{(6)}, A_{\mathrm{s}}^{(7)}, A_{\mathrm{s}}^{(8)}]^T$ consists of five unknown amplitudes of the displacement potentials. Elements of matrix **M** and vector **c** are given in Appendix C.

## 5 ENERGY PARTITIONS

We consider the energy balance or partition, calculating the energy flux, which is the scalar product of the traction and particle velocity across a surface element of unit area. The time average of the energy flux over a period defines the average energy intensity:

$$\left\langle E \right\rangle = \frac{1}{2} \mathrm{Re}(\tau_{zz} \dot{u}_z' + \tau_{xz} \dot{u}_x' - P_{\mathrm{f1}} \dot{w}_{1z}' - P_{\mathrm{f2}} \dot{w}_{2z}'), \tag{48}$$

where the tilde denotes complex conjugate, and $w_{1z}$ and $w_{2z}$ are the $z$-components of $\mathbf{w}^{(1)}$ and $\mathbf{w}^{(2)}$, respectively.

For an interface between two media, the energy partitions in medium $\Omega_1$ are obtained by solving a square matrix of order five as follows:

$$\left\langle \mathbf{E}^{\Omega_1} \right\rangle = \left\langle E_{ij}^{\Omega_1} \right\rangle = \frac{1}{2} \mathrm{Re}(\mathbf{X} \cdot \dot{\mathbf{Y}}'), \quad i, j = 0, 1, \ldots, 4, \tag{49}$$

where

$$\mathbf{X} = \begin{pmatrix} \tau_{zz}^{(0)} & \tau_{xz}^{(0)} & -P_{\mathrm{f1}}^{(0)} & -P_{\mathrm{f2}}^{(0)} \\ \tau_{zz}^{(1)} & \tau_{xz}^{(1)} & -P_{\mathrm{f1}}^{(1)} & -P_{\mathrm{f2}}^{(1)} \\ \tau_{zz}^{(2)} & \tau_{xz}^{(2)} & -P_{\mathrm{f1}}^{(2)} & -P_{\mathrm{f2}}^{(2)} \\ \tau_{zz}^{(3)} & \tau_{xz}^{(3)} & -P_{\mathrm{f1}}^{(3)} & -P_{\mathrm{f2}}^{(3)} \\ \tau_{zz}^{(4)} & \tau_{xz}^{(4)} & -P_{\mathrm{f1}}^{(4)} & -P_{\mathrm{f2}}^{(4)} \end{pmatrix}, \quad \mathbf{Y} = \begin{pmatrix} u_z^{(0)} & u_z^{(1)} & u_z^{(2)} & u_z^{(3)} & u_z^{(4)} \\ u_x^{(0)} & u_x^{(1)} & u_x^{(2)} & u_x^{(3)} & u_x^{(4)} \\ w_{1z}^{(0)} & w_{1z}^{(1)} & w_{1z}^{(2)} & w_{1z}^{(3)} & w_{1z}^{(4)} \\ w_{2z}^{(0)} & w_{2z}^{(1)} & w_{2z}^{(2)} & w_{2z}^{(3)} & w_{2z}^{(4)} \end{pmatrix}. \tag{50}$$

The diagonal components $\left\langle E_{ii}^{\Omega_1} \right\rangle$ identify the energy intensities of the incident wave ($i = 0$), and the reflected $P1$, $P2$, $P3$ and SV waves ($i = 1, 2, 3, 4$), whereas the off-diagonal components are the interaction energies, resulting from the interference between waves.

For the fluid, we have

$$\left\langle E \right\rangle = \frac{1}{2} \mathrm{Re}(-p_f \dot{U}_z'). \tag{51}$$

Hence, for a fluid/solid interface, we have

$$\left\langle \mathbf{E}^{\Omega_1} \right\rangle = \left\langle E_{ij}^{\Omega_1} \right\rangle = \frac{1}{2} \mathrm{Re}(\mathbf{X} \cdot \dot{\mathbf{Y}}'), \quad i, j = 0, 1, \tag{52}$$

where

$$\mathbf{X} = \begin{pmatrix} -p_{\mathrm{f}}^{(0)} \\ -p_{\mathrm{f}}^{(1)} \end{pmatrix}, \quad \mathbf{Y} = \begin{pmatrix} U_z^{(0)}, & U_z^{(1)} \end{pmatrix}. \tag{53}$$

Similarly, the corresponding matrix for medium $\Omega_2$ is

$$\left\langle \mathbf{E}^{\Omega_2} \right\rangle = \left\langle E_{ij}^{\Omega_2} \right\rangle = \frac{1}{2} \mathrm{Re}(\mathbf{C} \cdot \dot{\mathbf{D}}'), \quad i, j = 0, 1, 2, 3, \tag{54}$$

where

$$\mathbf{C} = \begin{pmatrix} \tau_{zz}^{(5)} & \tau_{xz}^{(5)} & -P_{\mathrm{f1}}^{(5)} & -P_{\mathrm{f2}}^{(5)} \\ \tau_{zz}^{(6)} & \tau_{xz}^{(6)} & -P_{\mathrm{f1}}^{(6)} & -P_{\mathrm{f2}}^{(6)} \\ \tau_{zz}^{(7)} & \tau_{xz}^{(7)} & -P_{\mathrm{f1}}^{(7)} & -P_{\mathrm{f2}}^{(7)} \\ \tau_{zz}^{(8)} & \tau_{xz}^{(8)} & -P_{\mathrm{f1}}^{(8)} & -P_{\mathrm{f2}}^{(8)} \end{pmatrix}, \quad \mathbf{D} = \begin{pmatrix} u_z^{(5)} & u_z^{(6)} & u_z^{(7)} & u_z^{(8)} \\ u_x^{(5)} & u_x^{(6)} & u_x^{(7)} & u_x^{(8)} \\ w_{1z}^{(5)} & w_{1z}^{(6)} & w_{1z}^{(7)} & w_{1z}^{(8)} \\ w_{2z}^{(5)} & w_{2z}^{(6)} & w_{2z}^{(7)} & w_{2z}^{(8)} \end{pmatrix}. \tag{55}$$

**Table 1.** Porous-medium properties.

| | $K_s$ (GPa) | $\mu_s$ (GPa) | $\rho_s$ (kg m$^{-3}$) | $\phi_{10}$ | $\phi_{20}$ | $c_1$ | $\kappa_1$ (darcy) | $\kappa_2$ (darcy) | $R_0$ (m) |
|---|---|---|---|---|---|---|---|---|---|
| Rock | 37.9 | 32.6 | 2650 | 0.25 | 0.32 | 11 | 0.1 | 100 | 0.01 |

**Table 2.** Fluid properties.

| | $K_{\mathrm{f}}$ (GPa) | $\eta_{\mathrm{f}}$ (Pa·s) | $\rho_{\mathrm{f}}$ (kg m$^{-3}$) |
|---|---|---|---|
| Water | 2.22 | 0.001 | 1000 |
| Gas | 0.0001 | $1.82 \times 10^{-5}$ | 1.2 |

In eq. (54), the sum of all the off-diagonal entries is the interaction energy resulting from the interference between four transmitted waves, whereas the diagonal elements $\left\langle E_{ii}^{\Omega_2} \right\rangle$ define the energy partition of the four transmitted waves in medium $\Omega_2$.

Then, we scale the energy intensities to that of the incident wave $\left\langle E_{00}^{\Omega_1} \right\rangle$, to obtain the energy ratios. In medium $\Omega_1$, the energy-ratio matrix $F_{ij}^{\Omega_1} = \left\langle E_{ij}^{\Omega_1} \right\rangle / \left\langle E_{00}^{\Omega_1} \right\rangle$ corresponds to the partition of energy among the incidence and reflected waves. Note that with $F_{00}^{\Omega_1} = 1$, the diagonal element $F_{ii}^{\Omega_1}$ ($i = 1, 2, 3, 4$, if $\Omega_1$ is a porous medium, and $i = 1$, if $\Omega_1$ is for a fluid) corresponds to the reflected waves, whereas the sum of all the other off-diagonal components corresponds to the partition among the incidence and reflected waves. Particularly, when $\Omega_1$ is a porous medium, the interference energy ratio of the incidence wave with the reflected waves $F_{IR}^{\Omega_1}$, and interference among the four reflected waves $F_{RR}^{\Omega_1}$, are

$$F_{IR}^{\Omega_1} = \sum_{i=1}^{4} \left( F_{i0}^{\Omega_1} + F_{0i}^{\Omega_1} \right), \quad \text{and} \quad F_{RR}^{\Omega_1} = \sum_{i=1}^{4} \sum_{j=1, j \neq i}^{4} F_{ij}^{\Omega_1}, \tag{56}$$

For the fluid half-space, the corresponding equations are

$$F_{IR}^{\Omega_1} = F_{10}^{\Omega_1} + F_{01}^{\Omega_1}, \quad \text{and} \quad F_{RR}^{\Omega_1} = 0. \tag{57}$$

A similar matrix $F_{ij}^{\Omega_2} = \left\langle E_{ij}^{\Omega_2} \right\rangle / \left\langle E_{00}^{\Omega_1} \right\rangle$ gives the energy partition among the four transmitted waves in the porous medium $\Omega_2$. The corresponding partition among the four transmitted waves is

$$F_{TT}^{\Omega_2} = \sum_{i=0}^{3} \sum_{j=0, j \neq i}^{3} F_{ij}^{\Omega_2}. \tag{58}$$

Energy conservation is satisfied as

$$\sum_{i=0}^{4} \sum_{j=0}^{4} F_{ij}^{\Omega_1} - \sum_{i=0}^{3} \sum_{j=0}^{3} F_{ij}^{\Omega_2} = 0, \tag{59}$$

for the interface between two porous media, and

$$\sum_{i=0}^{1} \sum_{j=0}^{1} F_{ij}^{\Omega_1} - \sum_{i=0}^{3} \sum_{j=0}^{3} F_{ij}^{\Omega_2} = 0, \tag{60}$$

for the interface between a fluid and a porous medium.

## 6 EXAMPLES

We consider the properties given in Table 1, taken from Tang *et al.* (2012) and Zhang *et al.* (2019). The fluid is assumed to be either gas or water, and its properties are given in Table 2 (Gurevich *et al.* 2004). Following Zhang *et al.* (2019), the volume fraction is $f_2 = \phi_2/\phi_{20}$, where $\phi_2 = \phi_c = 2\pi\varepsilon\gamma$ is the crack porosity, where $\varepsilon$ and $\gamma$ are the crack density and aspect ratio, respectively. Once $f_2$ is obtained, $f_1$ and $\phi_1$ can be determined. In the following, we assume $\varepsilon = 0.2$ and $\gamma = 0.002$ (Tang *et al.* 2012).

Fig. 3 shows the phase velocities of the four waves as a function of frequency, for gas- and water-saturated media. The $P1$-wave dissipation factor is displayed in Fig. 4. In the absence of LFF, the results are obtained by setting the inclusion radius $R_0$ equal to infinity. For the gas saturation case, the LFF mechanism hardly affects the wave propagation, since it induces negligible attenuation, as shown in Fig. 4(a). In contrast, when the fluid is water, the LFF mechanism induces a significant attenuation and dispersion of the $P1$-wave mode over [0.1, 10] kHz. The $P2$ wave is also affected and the dispersion effect occurs at higher frequencies. At very high frequencies, propagation is not affected by the LFF.

### 6.1 Interface between two porous media saturated with different fluids

We consider the gas–water contact (Dutta & Odé 1983) shown in Fig. 2(a), where incident $P1$ wave travels in the upper gas-saturated medium and is transmitted into the lower water-bearing medium. We assume the same properties in both layers as given in Table 1. We first investigate

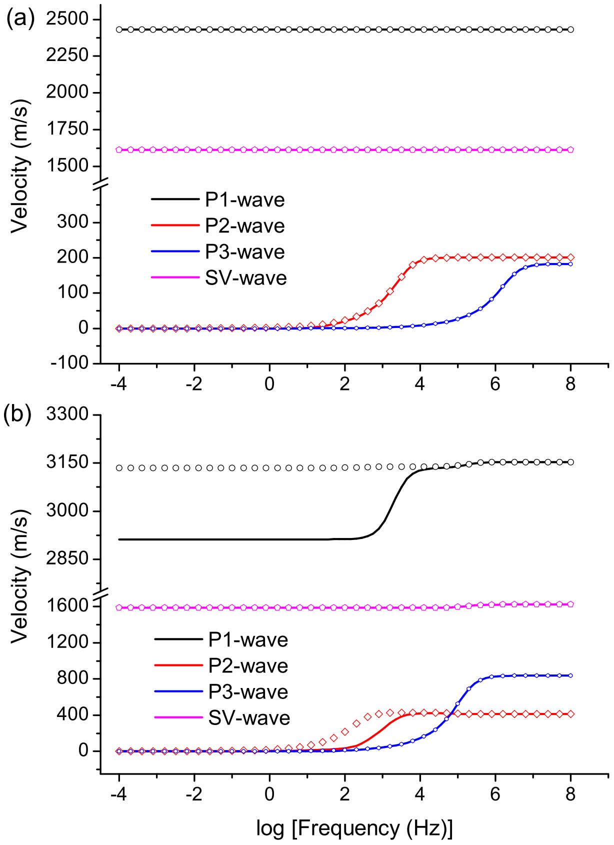

**Figure 3.** Phase velocities of the *P*1, SV, slow *P*2 and slow *P*3 waves as a function of frequency, for the gas-saturated (a) and water-bearing (b) media, respectively. The solid lines represent the results in the presence of local fluid flow (LFF), whereas open symbols only correspond to results without LFF.

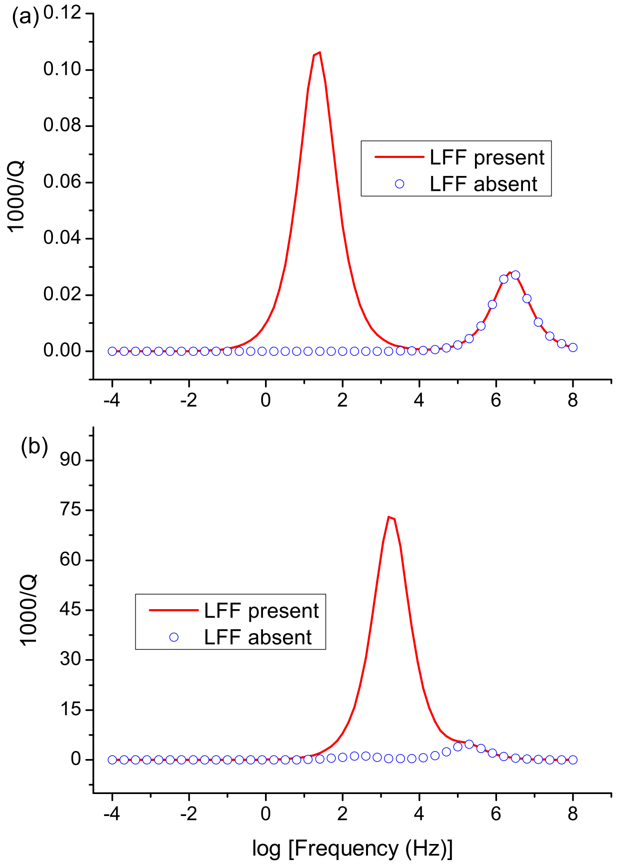

**Figure 4.** Dissipation factors of the fast *P*1 wave as a function of frequency, for the gas-saturated (a) and water-bearing (b) media.

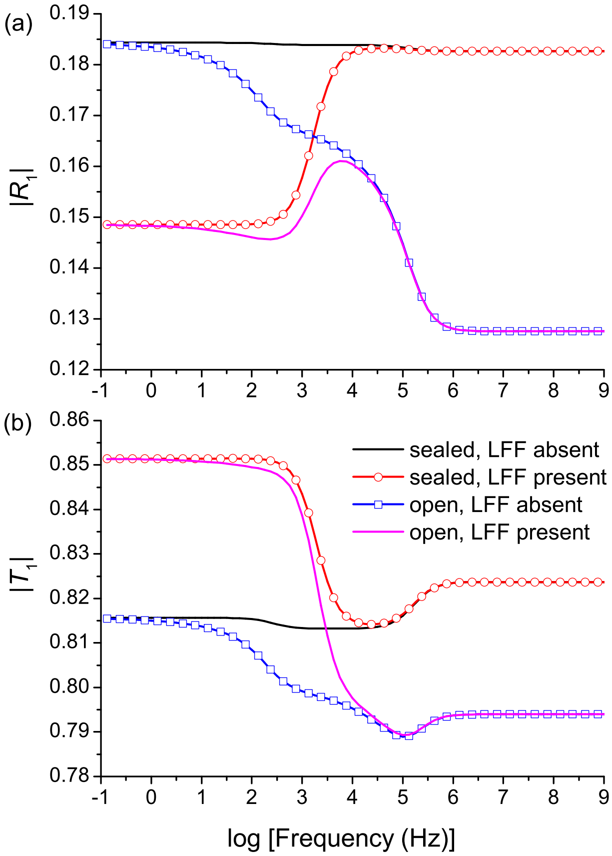

**Figure 5.** Magnitudes of the $P1$-wave reflection (a) and transmission (b) coefficients as a function of frequency at normal incidence.

the $R/T$ coefficients at normal incidence. Because the attenuation is negligible in the gas-saturated half-space, the inhomogeneity angle does not affect the propagation at the interface (Wang *et al.* 2020), and is set as $\gamma_0 = 45°$. Fig. 5 shows the magnitudes of the $P1$-wave coefficients as a function of frequency. We have omitted the results for the reflected and transmitted SV, $P2$ and $P3$ waves, since the SV-wave magnitudes are zero for all frequencies, and the $P2$- and P3-wave magnitudes are much smaller. We observe that the coefficients with open BCs differ from those with sealed BCs, and the difference increases with frequency. This effect was also reported in Qi *et al.* (2021). The LFF affects the propagation, causing a decreased $|R_1|$ at low frequencies for both open and sealed BCs. The reason can be attributed to the velocity dispersion at low frequencies (see Fig. 3b). The presence of LFF gives a lower $P1$-wave velocity in the water-bearing medium, and thus induces a smaller impedance contrast, causing the decrease in the reflected $P1$-wave magnitude. At high frequencies, the propagation is not affected by the LFF and the two results overlap.

The corresponding energy ratios are given in Fig. 6. We observe that, the main energy is transmitted as $P1$ wave. At low frequencies, the LFF affects the energy partitions, causing an enhanced transmitted $P1$-wave energy. The BCs affect the energy ratios in the same manner as the magnitudes. At high frequencies, the total reflected and transmitted $P1$-wave energy decreases, indicating that part of the energy is transferred to slow $P2$ and $P3$ waves, in agreement with the dispersion analysis. Also, the results of the open BCs exhibit a significantly decreased $P1$-wave energy (the absolute sum of $F_{11}^{\Omega_1}$ and $F_{11}^{\Omega_2}$) than those of the sealed BCs, suggesting that more $P1$-wave energy is transferred. This implies that the fluid flow across the interface enhances the energy transfer between slow and fast wave modes. The sum of all the energy ratios at the interface is –1, indicating that the conservation of energy is satisfied.

Next, we consider oblique incidence. Figs 7 and 8 show the magnitudes and energies of the reflected $P1$ and SV waves as a function of the incidence angle. For comparison, two different frequencies (10 Hz and 1 kHz) are considered. As expected from the dispersion analysis in Figs 3 and 4, at 10 Hz the two slow wave modes hardly propagate and the result is similar to that of two elastic media. Consequently, at 10 Hz, $|R_1|$ and $|R_4|$ are hardly affected by the BCs. In contrast, at 1 kHz, the slow $P2$ wave is wave-like and the porous effect is more significant.

The LFF affects wave propagation in a water-bearing medium, and hence the reflection and transmission. Specifically, the LFF mechanism generates a remarkable $P1$-wave attenuation at 1 kHz, and predicts a smaller $P1$-wave velocity. Consequently, the P1-wave impedance contrast decreases, which explains why the reflected $P1$-wave magnitude in the presence of LFF is smaller than that without LFF. The critical angle is also affected. For $f = 10$ Hz, the attenuation is negligible and both media behave elastically (lossless). The critical angle can be obtained as $\theta_c = \arcsin \dfrac{v_{p1}}{v_{p2}}$, where $v_{p1}$ and $v_{p2}$ are the $P1$-wave phase velocities in the upper and lower media. Because $v_{p2}$ is affected by the LFF, the critical angle also. Specially, at 10 Hz, we have $\theta_c = 50.8°$ and $\theta_c = 56.6°$, without and with LFF, respectively, in agreement with the angles where the discontinuity of $|R_1|$ firstly occurs. Rubino *et al.* (2006) alternatively defined a critical angle when the reflected absolute energy

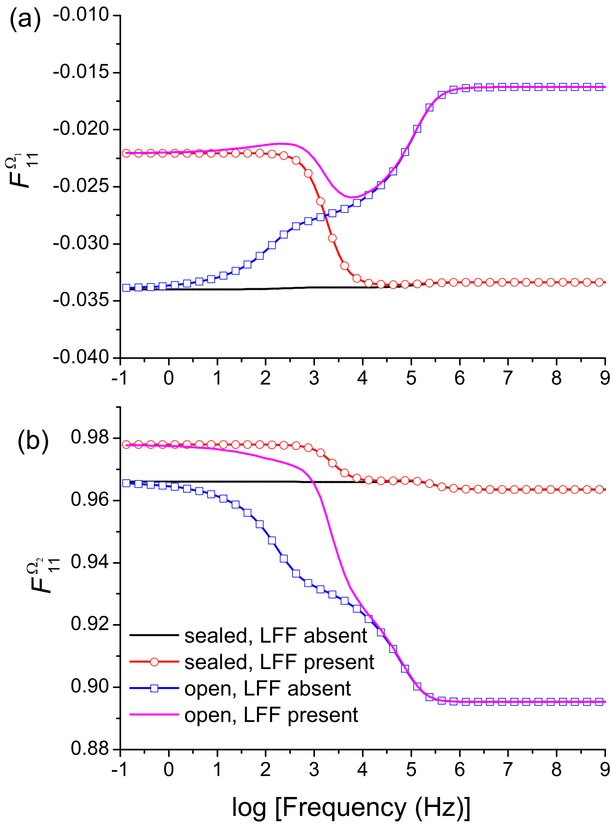

**Figure 6.** Energy ratios of the reflected (a) and transmitted (b) *P*1 waves as a function of frequency at normal incidence.

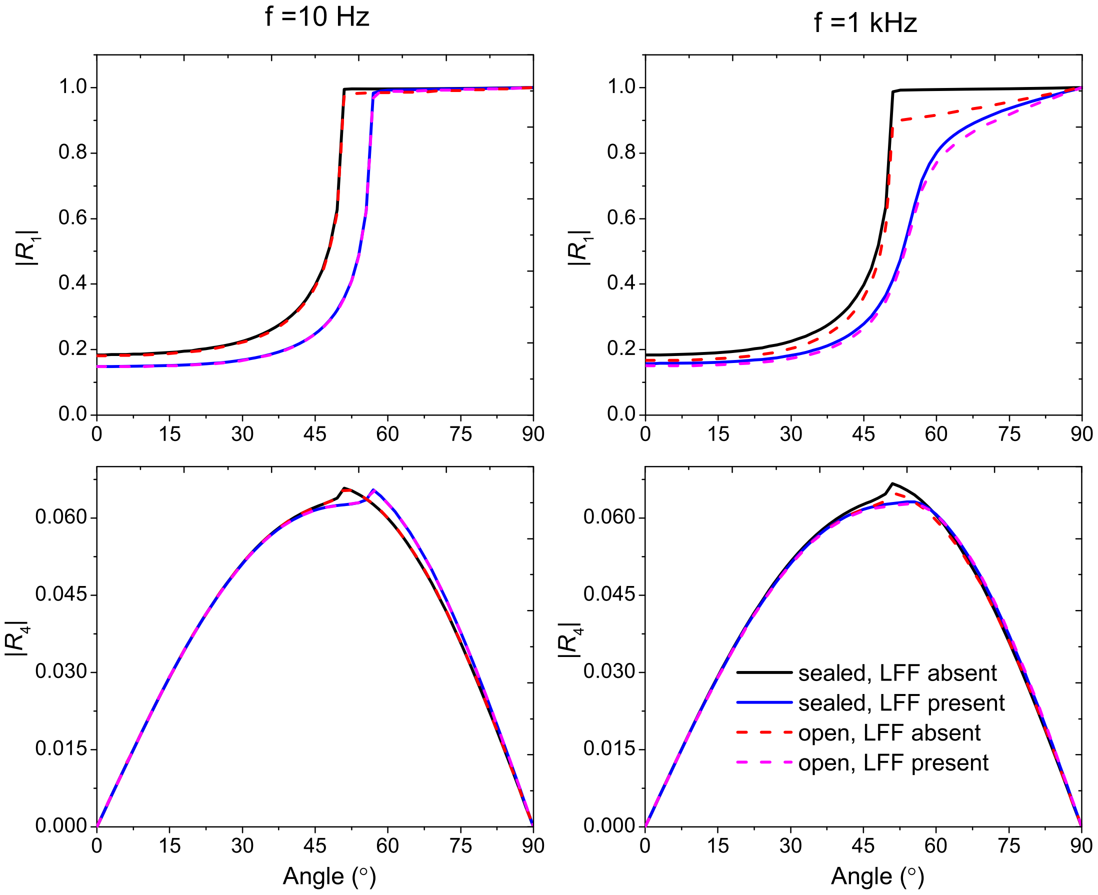

**Figure 7.** Magnitudes of the reflected *P*1 (upper) and SV (lower) waves as a function of incidence angle at 10 Hz (left-hand column) and 1 kHz (right-hand column).

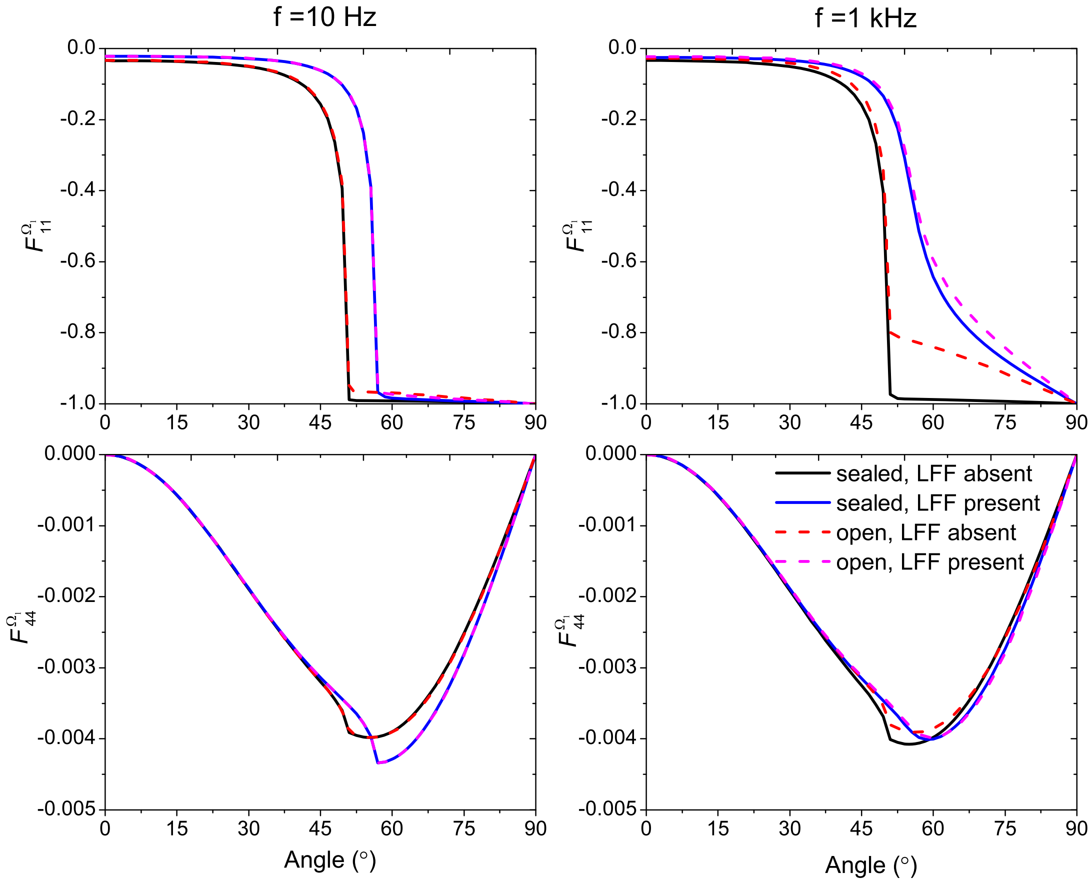

**Figure 8.** Energy ratios of the reflected $P1$ (upper two) and SV (lower two) waves as a function of incidence angle at 10 Hz (left-hand column) and 1 kHz (right-hand column).

ratio becomes 1. Variations of $F_{11}^{\Omega_1}$ with angle given in Fig. 8 confirm this fact. On the contrary, at $f = 1$ kHz, when the LFF is present, the medium behaves anelastically, implying that the transmitted wave is not confined to the interface but propagates into the medium (Sharma 2013). This explains the continuously increasing energy of the reflected P1 wave in the range [45°, 90°], in contrast to the discontinuity (the value increases sharply to 1) when the LFF is absent.

## 6.2 Interface between two porous media with different rock frames

Crack density and aspect ratio are two key parameters affecting wave propagation as shown in Fig. 9. We observe that, the larger the crack density the larger the dispersion and attenuation caused by mesoscopic flow, and the peak moves to low frequencies. In contrast, increasing the aspect ratio, attenuation and dispersion decrease, and the peak moves to high frequencies. At very high frequencies, the attenuation induced by the Biot global flow is nearly the same for all the crack porosities, since the global flow is mainly affected by the porosity of the host medium. It is evident that the crack density mainly affects the amount of attenuation, whereas the aspect ratio the location of the peak.

To investigate the influence of these two parameters on the scattering coefficients, we consider an interface between two water-bearing porous media having different crack density or aspect ratio, keeping all the other properties the same (see Table 1). We assume $\epsilon = 0.2$ and $\gamma = 0.002$ in the upper layer, different values in the lower layer, and the inhomogeneity angle is set to $\gamma_0 = 45°$. As shown in Fig. 10, where normal incidence has been assumed, if $\epsilon$ or $\gamma$ decreases, the $P1$-wave reflection magnitude at low frequencies increases, due to the fact that the $P1$-wave impedance contrast increases. There is dispersion between 0.1 and 10 kHz, due to the mesoscopic-flow attenuation. The difference between the sealed-pore and open-pore results is mainly observed at high frequencies, since at low frequencies the slow-wave modes are diffusive and become wavelike at high frequencies. Fig. 11 shows the reflection coefficient as a function of the incidence angle at 10 Hz and 1 kHz. Similarly, decreasing $\epsilon$ or $\gamma$ enhances the $P1$- and SV-wave reflection magnitudes at the same incidence angle. At 10 Hz, varying $\gamma$ induces a small velocity contrast, and smaller $P1$ and SV-wave reflection magnitudes, when compared with those induced by variations in $\epsilon$. At 1 kHz, the opposite behaviour for $P1$ wave occurs.

It is worth to note that, the present theory considers randomly oriented penny-shaped cracks, meaning that the rock is macroscopically isotropic. When the cracks are aligned, the rock can behave anisotropically. For example, Galvin & Gurevich (2009) considered a poroelastic medium with a distribution of aligned cracks and obtained frequency-dependent anisotropy and attenuation based on a multiple-scattering theory. Guo & Gurevich (2018) alternatively considered rocks containing two orthogonal sets of intersecting fractures, and confirmed this

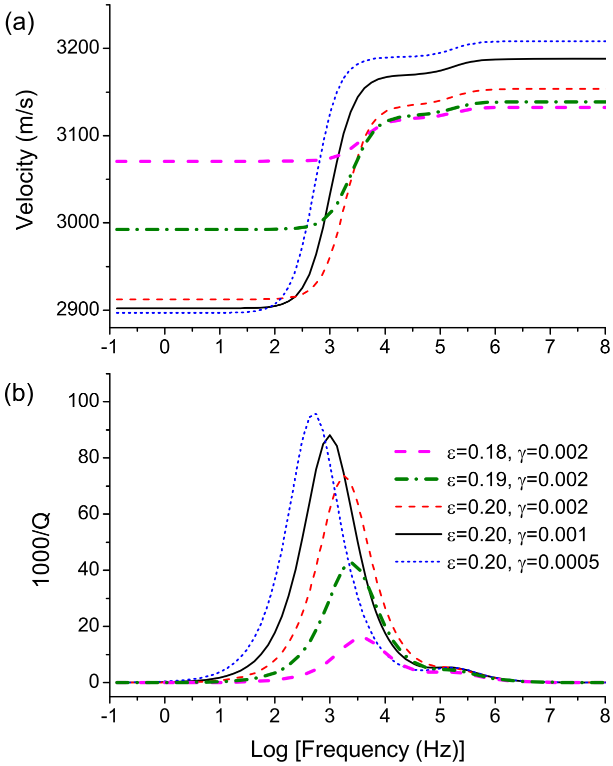

**Figure 9.** $P1$-wave velocity dispersion (a) and attenuation (b) for different crack densities $\epsilon$ and aspect ratios $\gamma$.

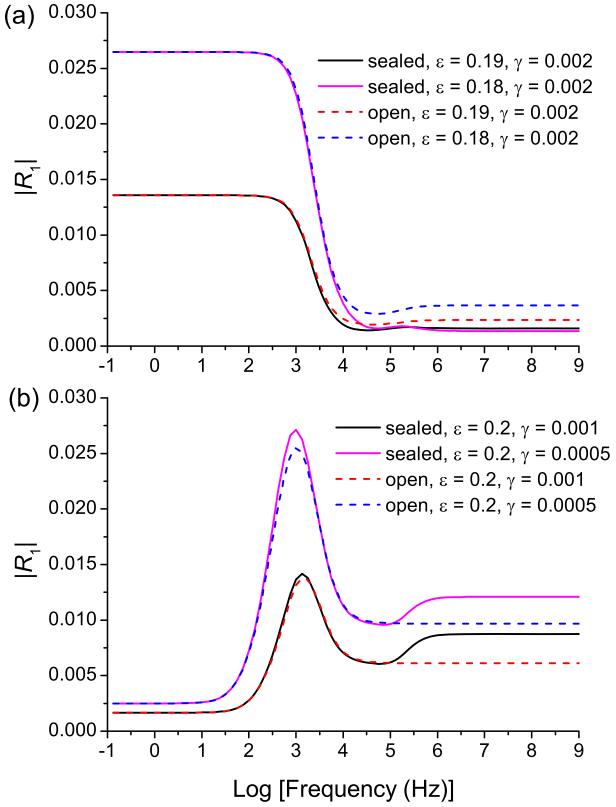

**Figure 10.** Magnitudes of the $P1$-wave reflection coefficients as a function of frequency at normal incidence for an interface separating two media with different (a) crack density $\epsilon$ or (b) aspect ratio $\gamma$ in the lower medium. We assume $\epsilon = 0.2$ and $\gamma = 0.002$ in the upper medium.

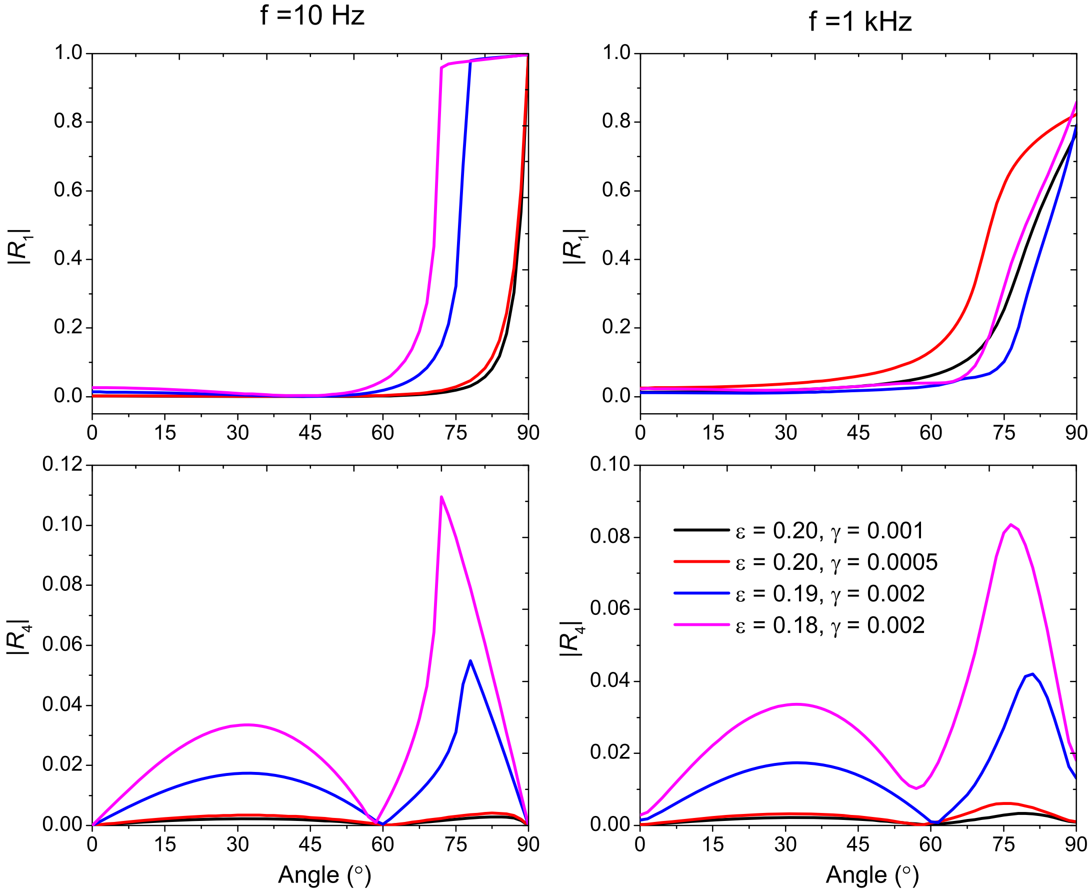

**Figure 11.** Magnitudes of the reflected $P1$ (upper panels) and SV (lower panels) waves as a function of incidence angle at 10 Hz (left-hand column) and 1 kHz (right-hand column), for different $\epsilon$ or $\gamma$ in the lower layer. We assume $\epsilon = 0.2$ and $\gamma = 0.002$ in the upper medium and open-pore boundary conditions are assumed.

frequency dependence. Jin *et al.* (2018) obtained similar results for aligned fractures and two immiscible fluids. In these cases, the reflections depend on frequency and azimuth.

### 6.3 Interface between water and a porous medium

Next, we consider water over a fluid-saturated medium, as displayed in Fig. 2(b). This occurs, for instance, when gas migrates from a hydrate formation into the sea (Pape *et al.* 2020). First, we consider that the lower medium is saturated with gas. Fig. 12 shows the reflection magnitude and corresponding energy ratio as a function of frequency at normal incidence. As explained by Qi *et al.* (2021), at normal incidence the sealed interface is equivalent to an interface between water and an effective elastic medium, with no frequency effects. On the contrary, the results for the open BCs depend on frequency and coincide with those of the sealed-pore case at low frequencies, less than $10^{-4}$ Hz. A similar case was investigated by Gurevich *et al.* (2004) based on Biot classical theory, where they conclude that the effect depends on the compressibility contrast between the gas and the fluid. At low frequencies, the $P3$ wave does not propagate and our case becomes equivalent to that of the Biot theory. This explains why Fig. 12 shows a similar trend to that of Gurevich *et al.* (2004). The LFF induces an additional (weak) attenuation peak, as illustrated in Fig. 4(a), and hence yields different results from those without LFF.

Fig. 13 shows the results at two different frequencies, where as in Fig. 12, the LFF has no effect when the interface is sealed. Two discontinuities occur at $\theta_1$ =37.8° and $\theta_2$ =67.6°. Because the sealed interface is equivalent to a water–elastic interface, these correspond to the critical angles at which the transmitted fast $P1$ wave and SV wave become evanescent. Contrarily, the results of the open-pore interface are affected by the LFF and are frequency dependent. The effect is mainly observed at low frequencies (10 Hz), as discussed in Fig. 12. A similar effect of BCs was observed by Denneman *et al.* (2002) using the classical Biot theory, due to the large impedance difference between water and gas. For the open-pore interface, the wave displacements in water are coupled to those in gas. The transmission coefficients are small at 1 kHz, while $|R_1|$ is close to 1. On the other hand, for the sealed-pore interface, the wave displacements in water are mainly coupled to those of the skeleton, and therefore we have dissimilar results compared to the open case, with the difference disappearing below $10^{-4}$ Hz.

Now, we consider water overlying a water-bearing medium. Fig. 14 shows the reflection magnitude and energy as a function of frequency for normal incidence. Unlike the gas-saturated case, the LFF affects the propagation in the water-bearing medium significantly, causing a decreased $P1$-wave velocity at low frequencies and significant dispersion in the range [0.1, 10] kHz, as shown in Fig. 3(b). Consequently,

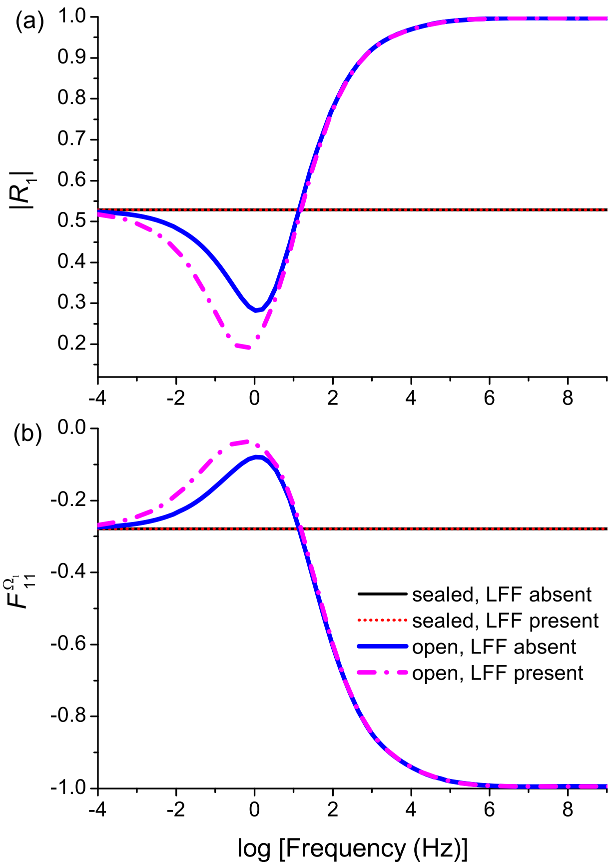

**Figure 12.** Magnitude (a) and energy ratio (b) of the reflected wave at normal incidence for an interface separating water and a gas-saturated medium.

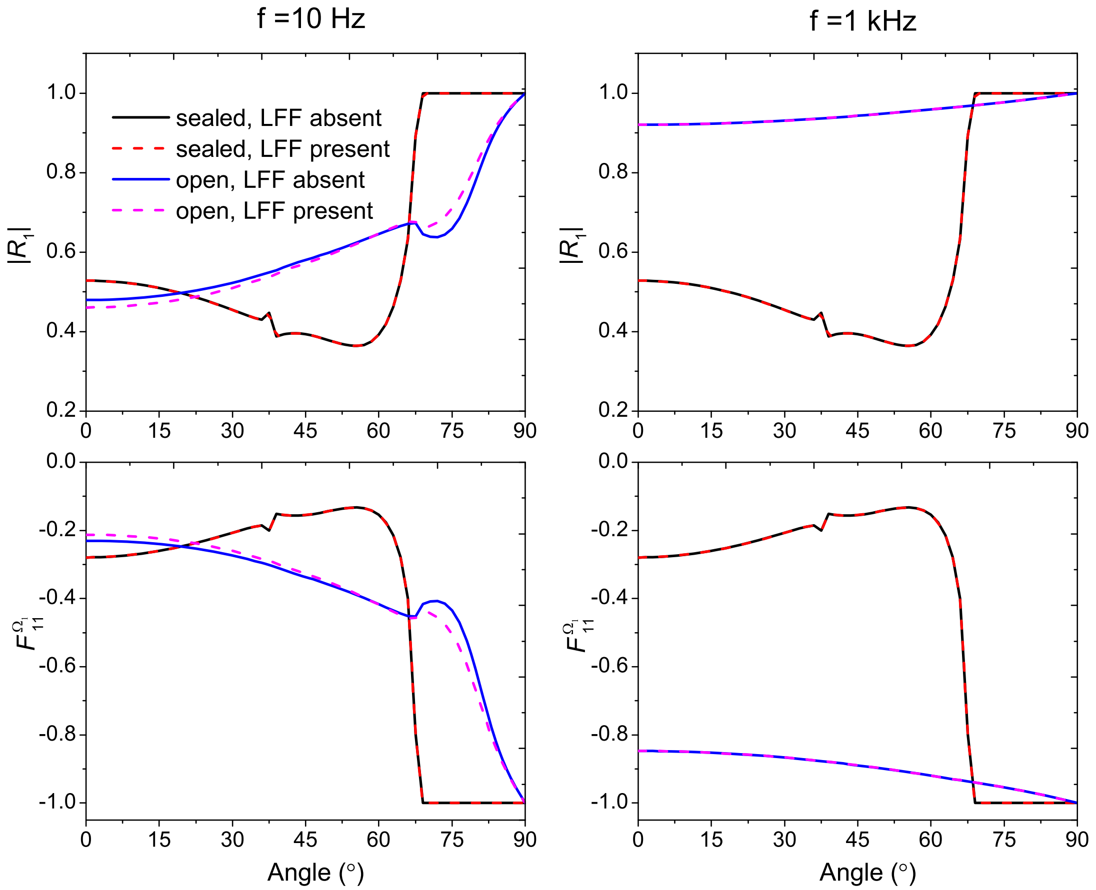

**Figure 13.** Magnitude (upper panels) and energy ratio (lower panels) of the reflected wave at 10 Hz (left-hand column) and 1 kHz (right-hand column), for an interface separating water and a gas-saturated medium.

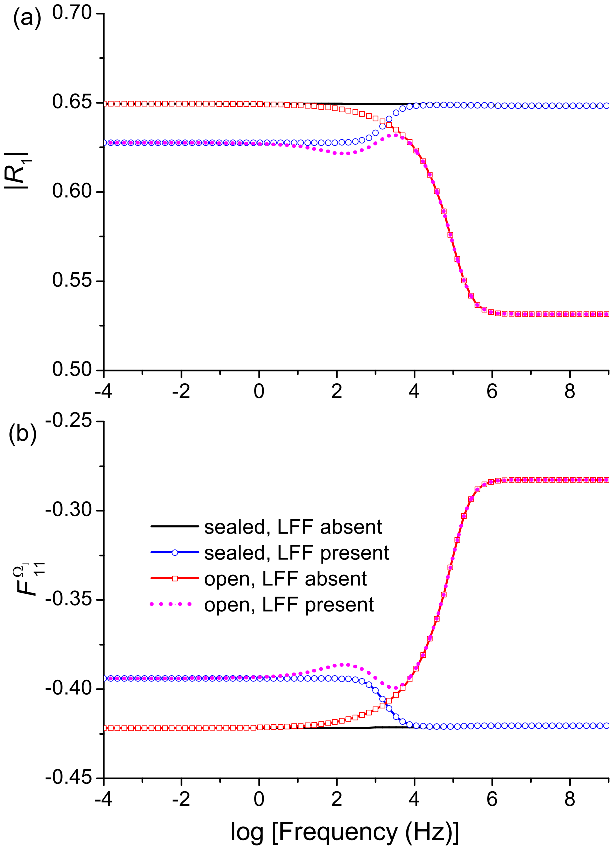

**Figure 14.** Magnitude (a) and energy ratio (b) of the reflected wave at normal incidence for an interface separating water and a water-bearing medium.

$|R_1|$ is smaller than that when the LFF is absent, since the $P1$-wave impedance contrast is decreased. In the open-pore case, more energy is transmitted at high frequencies. Fig. 15 shows the reflection magnitude and energy ratio as a function of the incidence angle for both sealed and open interfaces. At 10 Hz, the reflection coefficient is independent on the BCs. The result is in agreement with those in Fig. 3(b) in that the dispersion occurs at frequencies much higher than 10 Hz. The $P2$ and $P3$ waves hardly propagate and hence the medium behaves elastically (lossless). In contrast, at 1 kHz, the slow $P2$ wave becomes wavelike and the effects of the BCs are significant.

There are two discontinuities at $\theta_1 = 28.4^\circ$ and $\theta_2 = 70^\circ$in Fig. 15, associated with the transmitted $P1$- and SV-wave critical angles. At 10 Hz, these angles occur when the LFF is absent, whereas they become $\theta_1 = 31^\circ$ and $\theta_2 = 70^\circ$ if the LFF is present. The increase in $\theta_1$ is due to the fact that the LFF decreases the $P1$-wave velocity. For 1 kHz, the two angles are $\theta_1 = 28.4^\circ$ and $\theta_2 = 70^\circ$ when the LFF is absent and $\theta_1 = 30^\circ$ and $\theta_2 = 70^\circ$ if the LFF is present. When the frequency increases from 10 Hz to 1 kHz, the LFF increases the P1-wave velocity, thus causing the variation in $\theta_1$. At 1 kHz, $F_{11}^{\Omega_1}$ deviates from $-1$ for angles beyond $\theta_2$, implying that part of the energy is transmitted in the form of slow wave modes. The phenomenon is particularly evident when the interface is open.

## 7 CONCLUSIONS

We have analysed the reflection and transmission from interfaces between two fluid-saturated media, as well as between water and a fluid-saturated medium, including the effects of cracks. The poroelasticity equations are based on a generalization of the Biot-Rayleigh theory from spherical inclusions to the case of penny-shaped cracks, where the effect of mesoscopic local fluid flow (LFF) plays an important role. The theory predicts four wave modes, namely, a fast P1, two slow P2 and P3 and SV waves. The reflection coefficients and partitions of energy as a function of frequency and incidence angle are obtained, and the effects of LFF and BCs are studied. The examples reveal that the LFF attenuation mechanism affects the wave propagation in the water-bearing medium for frequencies lower than $10^4$ Hz, and hence the frequency and angle dependences of the reflection coefficients of the water–water-bearing medium interface and the gas–water contact, irrespective of the type of boundary condition. Differently, for the water–gas-saturated medium contact, the sealed interface is equivalent to a water–elastic (lossless) medium interface. The open-pore case coincides with the sealed-pore one at frequencies below $10^{-4}$ Hz. The crack density mainly affects the amount of attenuation, whereas the aspect ratio the location of the relaxation peak. Our findings provide insights for acquiring physical dependencies between reflection signatures and medium properties, which allows for frequency-dependent inversion for parameter estimations in cracked porous media.

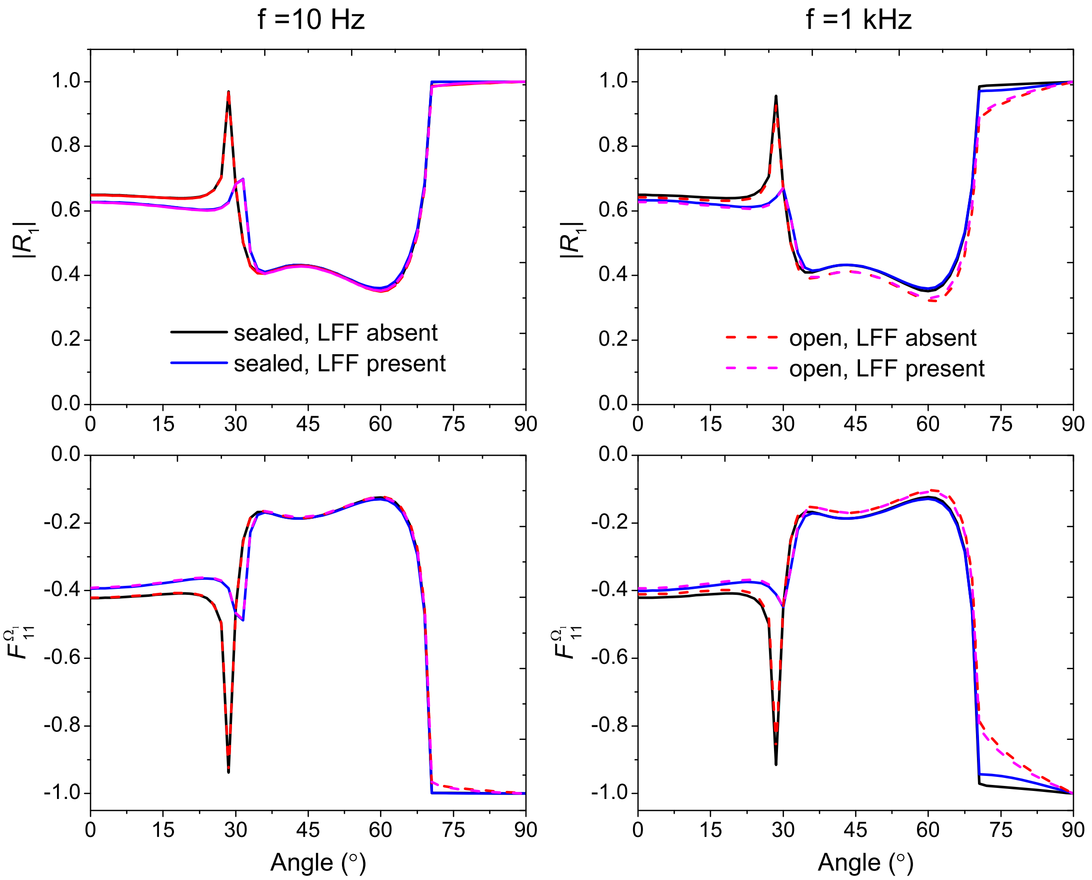

**Figure 15.** Magnitude (upper panels) and energy ratio (lower panels) of the reflected wave at 10 Hz (left-hand column) and 1 kHz (right-hand column), for an interface separating water and a water-bearing medium.

## ACKNOWLEDGMENTS

We are grateful to the editor, the assistant editor and two reviewers for their valuable comments. This work has been supported by the ‘National Nature Science Foundation of China (42174148, 41804095)’, the ‘China Postdoctoral Science Foundation (2020M682242)’ and the Postdoctoral Applied Research Project of Qingdao.

## DATA AVAILABILITY

Data and codes can be available by contacting the corresponding author.

## CONFLICT OF INTEREST

The authors declare that they have no conflict of interest.

## REFERENCES

Ba, J., Carcione, J.M. & Nie, J., 2011. Biot-Rayleigh theory of wave propagation in double-porosity media, *J. geophys. Res.,* **116**(B6), doi:10.1029/2010JB008185.

Berryman, J.G., 1979. Theory of elastic properties of composite materials, *Appl. Phys. Lett.,* **35**(11), 856–858.

Biot, M.A., 1956. Theory of propagation of elastic waves in a fluid-saturated porous solid. I. Low frequency range, *J. acoust. Soc. Am.,* **28**(2), 168–178.

Biot, M.A., 1962. Mechanics of deformation and acoustic propagation in porous media, *J. Appl. Phys.,* **33**(4), 1482–1498.

Borcherdt, R.D., 1982. Reflection-refraction of general P-and type-I S-waves in elastic and anelastic solids, *J. geophys. Int.,* **70**(3), 621–638.

Bouzidi, Y. & Schmitt, D.R., 2012. Incidence-angle-dependent acoustic reflections from liquid-saturated porous solids, *J. geophys. Int.,* **191**(3), 1427–1440.

Carcione, J.M., 2014. *Wave Fields in Real Media: Theory and Numerical Simulation of Wave Propagation in Anisotropic, Anelastic, Porous and Electromagnetic Media,* 3rd edn (extended and revised), Elsevier.

Carcione, J.M., Gei, D., Gurevich, B. & Ba, J., 2021. On the normal-incidence reflection coefficient in porous media, *Surv. Geophys.,* **42**(4), 923–942.

Carcione, J.M. & Gurevich, B., 2011. Differential form and numerical implementation of Biot’s poroelasticity equations with squirt dissipation, *Geophysics,* **76**(6), N55–N64.

Carcione, J.M., Morency, C. & Santos, J.E., 2010. Computational poroelasticity: a review, *Geophysics,* **75**(5), A229–A243.

Carcione, J.M. & Picotti, S., 2006. P-wave seismic attenuation by slow-wave diffusion: effects of inhomogeneous rock properties, *Geophysics,* **71**(3), O1–O8.

Chapman, M., Zatsepin, S.V. & Crampin, S., 2002. Derivation of a microstructural poroelastic model, *J. geophys. Int.,* **151**(2), 427–451.

Cui, Z. & Wang, K., 2003. Influence of the squirt flow on reflection and refraction of elastic waves at a fluid/fluid-saturated poroelastic solid interface, *Int. J. Eng. Sci.,* **41**(18), 2179–2191.

Dai, Z. & Kuang, Z., 2008. Reflection and transmission of elastic waves at the interface between water and a double porosity solid, *Transp. Porous Media,* **72**(3), 369–392.

Denneman, A.I., Drijkoningen, G.G., Smeulders, D.M. & Wapenaar, K., 2002. Reflection and transmission of waves at a fluid/porous-medium interface, *Geophysics,* **67**(1), 282–291.

Deresiewicz, H. & Rice, J.T., 1964. The effect of boundaries on wave propagation in a liquid-filled porous solid-V: transmission across plane interface, *Bull. seism. Soc. Am.,* **54**(1), 409–416.

Deresiewicz, H. & Skalak, R., 1963. On uniqueness in dynamic poroelasticity, *Bull. seism. Soc. Am.,* **53**(4), 783–788.

Dutta, N.C. & Odé, H., 1983. Seismic reflections from a gas-water contact, *Geophysics,* **48**(2), 148–162.

Dvorkin, J. & Nur, A., 1993. Dynamic poroelasticity: a unified model with the squirt and the Biot mechanisms, *Geophysics,* **58**(4), 524–533.

Fu, B., Guo, J., Fu, L.Y., Glubokovskikh, S., Galvin, R.J. & Gurevich, B., 2018. Seismic dispersion and attenuation in saturated porous rock with aligned slit cracks, *J. geophys. Res.,* **123**(8), 6890–6910.

Galvin, R.J. & Gurevich, B., 2009. Effective properties of a poroelastic medium containing a distribution of aligned cracks, *J. geophys. Res.,* **114**(B7), doi:10.1029/2008JB006032.

Guo, J. & Gurevich, B., 2020. Frequency-dependent P-wave anisotropy due to wave-induced fluid flow and elastic scattering in a fluid-saturated porous medium with aligned fractures, *J. geophys. Res.,* **125**(8), e2020JB020320, doi:10.1029/2020JB020320.

Guo, J., Rubino, J.G., Glubokovskikh, S. & Gurevich, B., 2018. Dynamic seismic signatures of saturated porous rocks containing two orthogonal sets of fractures: Theory versus numerical simulations, *J. geophys. Int.,* **213**(2), 1244–1262.

Gurevich, B., Ciz, R. & Denneman, A.I.M., 2004. Simple expressions for normal incidence reflection coefficients from an interface between fluid-saturated porous materials, *Geophysics,* **69**(6), 1372–1377.

Gurevich, B., Makarynska, D., de Paula, O.B. & Pervukhina, M., 2010. A simple model for squirt-flow dispersion and attenuation in fluid-saturated granular rocks, *Geophysics,* **75**(6), N109–N120.

Jin, Z., Chapman, M. & Papageorgiou, G., 2018. Frequency-dependent anisotropy in a partially saturated fractured rock, *J. geophys. Int.,* **215**(3), 1985–1998.

Kumari, M. & Kumar, M., 2020. Reflection of inhomogeneous waves at the surface of a cracked porous solid with penny-shaped inclusions, *Waves Rand. Complex Media,* **32**(4), 1–22.

Kumari, M. & Kumar, M., 2021. Wave-induced flow of pore fluid in a cracked porous solid containing penny-shaped inclusions, *Petrol. Sci.,* **18**(5), 1390–1408.

Liu, X., Li, H., Al-Shuhail, A.A., Liu, B. & Ren, Z., 2021. Reflection and transmission of plane waves at an interface separating two poro-viscoelastic materials with continuity and elastic consistence, *J. geophys. Int.,* **225**(2), 829–845.

Mavko, G. & Jizba, D., 1991. Estimating grain-scale fluid effects on velocity dispersion in rocks, *Geophysics,* **56**(12), 1940–1949.

Mavko, G. & Nur, A., 1975. Melt squirt in the asthenosphere, *J. geophys. Res.,* **80**(11), 1444–1448.

Müller, T.M., Gurevich, B. & Lebedev, M., 2010. Seismic wave attenuation and dispersion resulting from wave-induced flow in porous rocks-a review, *Geophysics,* **75**(5), 75A147–75A164.

Pape, T. *et al.*, 2020. Shallow gas hydrate accumulations at a Nigerian deepwater pockmark—quantities and dynamics, *J. geophys. Res.,* **125**(9), e2019JB018283, doi:10.1029/2019JB018283.

Pride, S.R. & Berryman, J.G., 2003a. Linear dynamics of double porosity dual-permeability materials. I. Governing equations and acoustic attenuation, *Phys. Rev. E,* **68**(3), doi:10.1103/PhysRevE.68.036603.

Pride, S.R. & Berryman, J.G., 2003b. Linear dynamics of double porosity dual-permeability materials. II. Fluid transport equations, *Phys. Rev. E,* **68**(3), doi:10.1103/PhysRevE.68.036604.

Pride, S.R., Berryman, J.G. & Harris, J.M., 2004. Seismic attenuation due to wave-induced flow, *J. geophys. Res.,* **109**(B1), doi:10.1029/2003JB002639.

Qi, Q., Cao, J., Wang, X. & Gao, J., 2021. Influence of interface condition on reflection of elastic waves in fluid-saturated porous media, *Geophysics,* **86**(4), MR223–MR233.

Rubino, J.G., Ravazzoli, C.L. & Santos, J.E., 2006. Reflection and transmission of waves in composite porous media: a quantification of energy conversions involving slow waves, *J. acoust. Soc. Am.,* **120**(5), 2425–2436.

Russell, B.H., Gray, D. & Hampson, D.P., 2011. Linearized AVO and poroelasticity, *Geophysics,* **76**(3), C19–C29.

Santos, J.E., Corbero, J.M., Ravazzoli, C.L. & Hensley, J.L., 1992. Reflection and transmission coefficients in fluid-saturated porous media, *J. acoust. Soc. Am.,* **91**(4), 1911–1923.

Sharma, M.D., 2013. Effect of local fluid flow on reflection of plane elastic waves at the boundary of a double-porosity medium, *Adv. Water Resour.,* **61,** 62–73.

Tang, X., 2011. A unified theory for elastic wave propagation through porous media containing cracks—an extension of Biot's poroelastic wave theory, *Sci. China Earth Sci.,* **54**(9), 1441–1452.

Tang, X., Chen, X. & Xu, X., 2012. A cracked porous medium elastic wave theory and its application to interpreting acoustic data from tight formations, *Geophysics,* **77**(6), D245–D252.

Thomsen, L., 1985. Biot-consistent elastic moduli of porous rocks: low-frequency limit, *Geophysics,* **50**(12), 2797–2807.

Wang, E., Carcione, J.M., Ba, J. & Liu, Y., 2020. Reflection and transmission of plane elastic waves at an interface between two double-porosity media: effect of local fluid flow, *Surv. Geophys.,* **41**(2), 283–322.

Xu, D., Han, T. & Fu, L.Y., 2021. Seismic dispersion and attenuation in layered porous rocks with fractures of varying orientations, *Geophys. Prospect.,* **69**(1), 220–235.

Zhang, L., Ba, J., Carcione, J.M. & Sun, W., 2019. Modeling wave propagation in cracked porous media with penny-shaped inclusions, *Geophysics,* **84**(4), WA141–WA151.

Zhao, L., Han, D.H., Yao, Q., Zhou, R. & Yan, F., 2015. Seismic reflection dispersion due to wave-induced fluid flow in heterogeneous reservoir rocks, *Geophysics,* **80**(3), D221–D235.

Zong, Z., Yin, X. & Wu, G., 2012. AVO inversion and poroelasticity with P- and S-wave moduli, *Geophysics,* **77**(6), N17–N24.

## APPENDIX A: EXPRESSIONS OF THE STIFFNESS AND DENSITY COEFFICIENTS

Following Zhang *et al.* (2019), the stiffness coefficients in eq. (4) are

$$\begin{aligned}
\lambda_c &= (1-\phi)\,K_s - \frac{2}{3}\mu_b + \left(2 - \frac{K_s}{K_f}\right)(\phi_1\alpha_1 M_1 + \phi_2\alpha_2 M_2) - \left(1 - \frac{K_s}{K_f}\right)\left(\phi_1^2 M_1 + \phi_2^2 M_2\right),\\
\alpha_1 &= \frac{\beta\phi_1 K_s}{\gamma K_f} + \phi_1, \quad \alpha_2 = \frac{\phi_2 K_s}{\gamma K_f} + \phi_2,\\
M_1 &= \frac{K_f}{(\beta/\gamma + 1)\,\phi_1}, \quad M_2 = \frac{K_f}{(1/\gamma + 1)\,\phi_2},\\
\gamma &= \frac{K_s}{K_f}\left[\frac{\beta\phi_1 + \phi_2}{1 - \phi - K_b/K_s}\right], \quad \beta = \frac{\phi_{20}}{\phi_{10}}\left[\frac{1-(1-\phi_{10})\,K_s/K_{b1}}{1-(1-\phi_{20})\,K_s/K_{b2}}\right],
\end{aligned} \tag{A1}$$

where $\phi = \phi_1 + \phi_2$ is the total porosity, $K_s$ and $K_f$ are the bulk moduli of the solid and fluid, $K_b$ is the dry-rock modulus, which should be Biot consistent (Thomsen 1985):

$$K_b = \frac{2}{3}\frac{1+v_B}{1-2v_B}\mu_b, \tag{A2}$$

with $\mu_b = \mu_s\left(1 - \frac{\phi_1}{1-b_B} - B_B\varepsilon\right)$, $b_B = \frac{2}{15}\frac{4-5v_B}{1-v_B}$ and $B_B = \frac{32}{45}\frac{(1-v_B)(5-v_B)}{2-v_B}$, where $\mu_s$ is the grain shear modulus, $v_B$ is the Poisson ratio, and $\varepsilon$ is the crack density; $K_{b1}$ and $K_{b2}$ are the dry-rock bulk moduli of the host medium and inclusions, which can be determined by

$$K_{b1} = \frac{(1-\phi_{10})K_s}{1+c_1\phi_{10}}, \quad \frac{f_2}{K_{b2}} = \frac{1}{K_b} - \frac{f_1}{K_{b1}}, \tag{A3}$$

where $c_1$ is the consolidation parameter of the host medium.

In the uniform-porosity case, we have

$$\begin{aligned}
A &= (1-\phi)K_s - 2N/3 - K_s(Q_1+Q_2)/K_f, \quad N = \mu_b,\\
Q_1 &= \alpha_1 M_1\phi_1 - M_1\phi_1^2, \quad R_1 = M_1\phi_1^2,\\
Q_2 &= \alpha_2 M_2\phi_2 - M_2\phi_2^2, \quad R_2 = M_2\phi_2^2.
\end{aligned} \tag{A4}$$

The five density coefficients $\rho_{ij}$ in eq. (10), defined in the same manner as Biot (1962), are

$$\begin{aligned}
\rho_{00} &= (1-\phi)\rho_s - \rho_f(\phi-1)/2,\\
\rho_{11} &= (\phi_1 + f_1)\rho_f/2, \quad \rho_{22} = (\phi_2 + f_2)\rho_f/2,\\
\rho_{01} &= (\phi_1 - f_1)\rho_f/2, \quad \rho_{02} = (\phi_2 - f_2)\rho_f/2.
\end{aligned} \tag{A5}$$

## APPENDIX B: COMPONENTS OF G AND e IN EQ. (39)

By defining

$$\begin{aligned}
n_1 &= \lambda_c - \alpha_1 M_1\phi_1 - \alpha_2 M_2\phi_2 + d_1(\alpha_1 M_1\phi_1\phi_2 - \alpha_2 M_2\phi_1\phi_2),\\
n_2 &= \alpha_1 M_1\phi_1 + d_2(\alpha_1 M_1\phi_1\phi_2 - \alpha_2 M_2\phi_1\phi_2),\\
n_3 &= \alpha_2 M_2\phi_2 + d_3(\alpha_1 M_1\phi_1\phi_2 - \alpha_2 M_2\phi_1\phi_2),\\
h_1 &= -\alpha_1 M_1 + M_1\phi_1 - M_1\phi_1\phi_2 d_1,\\
h_2 &= -M_1\phi_1 - M_1\phi_1\phi_2 d_2,\\
h_3 &= -M_1\phi_1\phi_2 d_3,\\
g_1 &= -\alpha_2 M_2 + M_2\phi_2 + M_2\phi_1\phi_2 d_1,\\
g_2 &= M_2\phi_1\phi_2 d_2,\\
g_3 &= -M_2\phi_2 + M_2\phi_1\phi_2 d_3,
\end{aligned} \tag{B1}$$

the components of matrix **G** can be expressed by

$$\begin{aligned}
&G_{11} = 2\bar{\mu}p_1q_1, \quad G_{12} = 2\bar{\mu}p_2q_2, \quad G_{13} = 2\bar{\mu}p_3q_3, \quad G_{14} = \bar{\mu}(p_4^2 - q_4^2),\\
&G_{15} = 2\mu p_5q_5, \quad G_{16} = 2\mu p_6q_6, \quad G_{17} = 2\mu p_7q_7, \quad G_{18} = -\mu(p_8^2 - q_8^2),
\end{aligned} \tag{B2}$$

$$\begin{aligned}
&G_{21} = 2\bar{\mu} q_1^2 + (\bar{n}_1 + \bar{n}_2\bar{\nu}_1 + \bar{n}_3\bar{\delta}_1)(p_1^2 + q_1^2),\\
&G_{22} = 2\bar{\mu} q_2^2 + (\bar{n}_1 + \bar{n}_2\bar{\nu}_2 + \bar{n}_3\bar{\delta}_2)(p_2^2 + q_2^2),\\
&G_{23} = 2\bar{\mu} q_3^2 + (\bar{n}_1 + \bar{n}_2\bar{\nu}_3 + \bar{n}_3\bar{\delta}_3)(p_3^2 + q_3^2),\\
&G_{24} = 2\bar{\mu} p_4 q_4,\\
&G_{25} = -\left[2\mu q_5^2 + (n_1 + n_2\nu_1 + n_3\delta_1)(p_5^2 + q_5^2)\right],\\
&G_{26} = -\left[2\mu q_6^2 + (n_1 + n_2\nu_2 + n_3\delta_2)(p_6^2 + q_6^2)\right],\\
&G_{27} = -\left[2\mu q_7^2 + (n_1 + n_2\nu_3 + n_3\delta_3)(p_7^2 + q_7^2)\right],\\
&G_{28} = 2\mu p_8 q_8,
\end{aligned} \tag{B3}$$

$$\begin{aligned}
&G_{31} = p_1,\quad G_{32} = p_2,\quad G_{33} = p_3,\quad G_{34} = -q_4,\\
&G_{35} = -p_5,\quad G_{36} = -p_6,\quad G_{37} = -p_7,\quad G_{38} = -q_8,
\end{aligned} \tag{B4}$$

$$\begin{aligned}
&G_{41} = q_1,\quad G_{42} = q_2,\quad G_{43} = q_3,\quad G_{44} = p_4,\\
&G_{45} = q_5,\quad G_{46} = q_6,\quad G_{47} = q_7,\quad G_{48} = -p_8,
\end{aligned} \tag{B5}$$

$$\begin{aligned}
&G_{51} = \bar{\phi}_1(\bar{\nu}_1 - 1)q_1,\ G_{52} = \bar{\phi}_1(\bar{\nu}_2 - 1)q_2,\ G_{53} = \bar{\phi}_1(\bar{\nu}_3 - 1)q_3,\ G_{54} = \bar{\phi}_1(\bar{\nu}_4 - 1)p_4,\\
&G_{55} = \phi_1(\nu_1 - 1)q_5,\ G_{56} = \phi_1(\nu_2 - 1)q_6,\ G_{57} = \phi_1(\nu_3 - 1)q_7,\ G_{58} = -\phi_1(\nu_4 - 1)p_8,
\end{aligned} \tag{B6}$$

$$\begin{aligned}
&G_{61} = \bar{\phi}_2(\bar{\delta}_1 - 1)q_1,\ G_{62} = \bar{\phi}_2(\bar{\delta}_2 - 1)q_2,\ G_{63} = \bar{\phi}_2(\bar{\delta}_3 - 1)q_3,\ G_{64} = \bar{\phi}_2(\bar{\delta}_4 - 1)p_4,\\
&G_{65} = \phi_2(\delta_1 - 1)q_5,\ G_{66} = \phi_2(\delta_2 - 1)q_6,\ G_{67} = \phi_2(\delta_3 - 1)q_7,\ G_{68} = -\phi_2(\delta_4 - 1)p_8,
\end{aligned} \tag{B7}$$

$$\begin{aligned}
&G_{71} = (p_1^2 + q_1^2)(\bar{h}_1 + \bar{h}_2\bar{\nu}_1 + \bar{h}_3\bar{\delta}_1),\quad G_{72} = (p_2^2 + q_2^2)(\bar{h}_1 + \bar{h}_2\bar{\nu}_2 + \bar{h}_3\bar{\delta}_2),\\
&G_{73} = (p_3^2 + q_3^2)(\bar{h}_1 + \bar{h}_2\bar{\nu}_3 + \bar{h}_3\bar{\delta}_3),\quad G_{74} = 0,\\
&G_{75} = -\left[(p_5^2 + q_5^2)(h_1 + h_2\nu_1 + h_3\delta_1) + Z_I\phi_1(\nu_1 - 1)q_5\right],\\
&G_{76} = -\left[(p_6^2 + q_6^2)(h_1 + h_2\nu_2 + h_3\delta_2) + Z_I\phi_1(\nu_2 - 1)q_6\right],\\
&G_{77} = -\left[(p_7^2 + q_7^2)(h_1 + h_2\nu_3 + h_3\delta_3) + Z_I\phi_1(\nu_3 - 1)q_7\right],\\
&G_{78} = Z_I\phi_1(\nu_4 - 1)p_8,
\end{aligned} \tag{B8}$$

$$\begin{aligned}
&G_{81} = (p_1^2 + q_1^2)(\bar{g}_1 + \bar{g}_2\bar{\nu}_1 + \bar{g}_3\bar{\delta}_1),\quad G_{82} = (p_2^2 + q_2^2)(\bar{g}_1 + \bar{g}_2\bar{\nu}_2 + \bar{g}_3\bar{\delta}_2),\\
&G_{83} = (p_3^2 + q_3^2)(\bar{g}_1 + \bar{g}_2\bar{\nu}_3 + \bar{g}_3\bar{\delta}_3),\quad G_{84} = 0,\\
&G_{85} = -\left[(p_5^2 + q_5^2)(g_1 + g_2\nu_1 + g_3\delta_1) + Z_I\phi_2(\delta_1 - 1)q_5\right],\\
&G_{86} = -\left[(p_6^2 + q_6^2)(g_1 + g_2\nu_2 + g_3\delta_2) + Z_I\phi_2(\delta_2 - 1)q_6\right],\\
&G_{87} = -\left[(p_7^2 + q_7^2)(g_1 + g_2\nu_3 + g_3\delta_3) + Z_I\phi_2(\delta_3 - 1)q_7\right],\\
&G_{88} = Z_I\phi_2(\delta_4 - 1)p_8,
\end{aligned} \tag{B9}$$

where variables with and without a bar correspond to quantities of the upper and lower half-spaces, respectively.

The components of **e** are

$$\begin{aligned}
&e_1 = 2\bar{\mu} p_0 q_0 A_{\mathrm{s}}^{(0)},\\
&e_2 = -\left[2\bar{\mu} q_0^2 + (\bar{n}_1 + \bar{n}_2\bar{\nu}_1 + \bar{n}_3\bar{\delta}_1)(p_0^2 + q_0^2)\right] A_{\mathrm{s}}^{(0)},\\
&e_3 = -p_0 A_{\mathrm{s}}^{(0)},\\
&e_4 = q_0 A_{\mathrm{s}}^{(0)},\\
&e_5 = \bar{\phi}_1(\bar{\nu}_1 - 1)q_0 A_{\mathrm{s}}^{(0)},\\
&e_6 = \bar{\phi}_2(\bar{\delta}_1 - 1)q_0 A_{\mathrm{s}}^{(0)},\\
&e_7 = -(p_0^2 + q_0^2)(\bar{h}_1 + \bar{h}_2\bar{\nu}_1 + \bar{h}_3\bar{\delta}_1)A_{\mathrm{s}}^{(0)},\\
&e_8 = -(p_0^2 + q_0^2)(\bar{g}_1 + \bar{g}_2\bar{\nu}_1 + \bar{g}_3\bar{\delta}_1)A_{\mathrm{s}}^{(0)}.
\end{aligned} \tag{B10}$$

When $Z_I$ is zero, the equations correspond to the open BCs, whereas $Z_I = \infty$ to sealed BCs.

## APPENDIX C: COMPONENTS OF M AND c IN EQ. (47)

The elements of matrix **M** are

$$M_{11} = 0,\quad M_{12} = 2p_5 q_5,\quad M_{13} = 2p_6 q_6,\quad M_{14} = 2p_7 q_7,\quad M_{15} = -(p_8^2 - q_8^2), \tag{C1}$$

$$\begin{aligned}
&M_{21} = \bar{K}_{\mathrm{f}}(p_0^2 + q_0^2),\quad M_{22} = -\left[2\mu q_5^2 + (n_1 + n_2\nu_1 + n_3\delta_1)(p_5^2 + q_5^2)\right],\\
&M_{23} = -\left[2\mu q_6^2 + (n_1 + n_2\nu_2 + n_3\delta_2)(p_6^2 + q_6^2)\right],\\
&M_{24} = -\left[2\mu q_7^2 + (n_1 + n_2\nu_3 + n_3\delta_3)(p_7^2 + q_7^2)\right],\quad M_{25} = 2\mu p_8 q_8,
\end{aligned} \tag{C2}$$

$$\begin{aligned}
&M_{31} = q_0,\quad M_{32} = \left[1 + \phi_1(\nu_1 - 1) + \phi_2(\delta_1 - 1)\right] q_5,\\
&M_{33} = \left[1 + \phi_1(\nu_2 - 1) + \phi_2(\delta_2 - 1)\right] q_6,\\
&M_{34} = \left[1 + \phi_1(\nu_3 - 1) + \phi_2(\delta_3 - 1)\right] q_7,\\
&M_{35} = -\left[1 + \phi_1(\nu_4 - 1) + \phi_2(\delta_4 - 1)\right] p_8,
\end{aligned} \tag{C3}$$

$$\begin{aligned}
M_{41} &= -\bar{K}_{\mathrm{f}}(p_0^2+q_0^2),\\
M_{42} &= -\left[(p_5^2+q_5^2)(h_1+h_2\nu_1+h_3\delta_1)+Z_I\phi_1(\nu_1-1)q_5\right],\\
M_{43} &= -\left[(p_6^2+q_6^2)(h_1+h_2\nu_2+h_3\delta_2)+Z_I\phi_1(\nu_2-1)q_6\right],\\
M_{44} &= -\left[(p_7^2+q_7^2)(h_1+h_2\nu_3+h_3\delta_3)+Z_I\phi_1(\nu_3-1)q_7\right],\\
M_{45} &= Z_I\phi_1(\nu_4-1)p_8,
\end{aligned} \tag{C4}$$

$$\begin{aligned}
M_{51} &= -\bar{K}_{\mathrm{f}}(p_0^2+q_0^2),\\
M_{52} &= -\left[(p_5^2+q_5^2)(g_1+g_2\nu_1+g_3\delta_1)+Z_I\phi_2(\delta_1-1)q_5\right],\\
M_{53} &= -\left[(p_6^2+q_6^2)(g_1+g_2\nu_2+g_3\delta_2)+Z_I\phi_2(\delta_2-1)q_6\right],\\
M_{54} &= -\left[(p_7^2+q_7^2)(g_1+g_2\nu_3+g_3\delta_3)+Z_I\phi_2(\delta_3-1)q_7\right],\\
M_{55} &= Z_I\phi_2(\delta_4-1)p_8.
\end{aligned} \tag{C5}$$

The components of **c** are

$$\begin{aligned}
c_1 &= 0,\\
c_2 &= -\bar{K}_{\mathrm{f}}(p_0^2+q_0^2)A_{\mathrm{s}}^{(0)},\\
c_3 &= q_0A_{\mathrm{s}}^{(0)},\\
c_4 &= \bar{K}_{\mathrm{f}}(p_0^2+q_0^2)A_{\mathrm{s}}^{(0)},\\
c_5 &= \bar{K}_{\mathrm{f}}(p_0^2+q_0^2)A_{\mathrm{s}}^{(0)}.
\end{aligned} \tag{C6}$$